PAPER

Check for updates

Mechanical properties of cell- and microgel bead-laden oxidized alginate-gelatin hydrogels†

T. Distler, [ID] *‡[a] L. Kretzschmar,‡[b] D. Schneidereit,[c] S. Girardo, [ID] [d] R. Goswami, [ID] [d] O. Friedrich, [ID] [c] R. Detsch,[a] J. Guck,[d,e] A. R. Boccaccini [ID] *[a] and S. Budday [ID] *[b]

3D-printing technologies, such as biofabrication, capitalize on the homogeneous distribution and growth of cells inside biomaterial hydrogels, ultimately aiming to allow for cell differentiation, matrix remodeling, and functional tissue analogues. However, commonly, only the mechanical properties of the bioinks or matrix materials are assessed, while the detailed influence of cells on the resulting mechanical properties of hydrogels remains insufficiently understood. Here, we investigate the properties of hydrogels containing cells and spherical PAAm microgel beads through multi-modal complex mechanical analyses in the small- and large-strain regimes. We evaluate the individual contributions of different filler concentrations and a non-fibrous oxidized alginate-gelatin hydrogel matrix on the overall mechanical behavior in compression, tension, and shear. Through material modeling, we quantify parameters that describe the highly nonlinear mechanical response of soft composite materials. Our results show that the stiffness significantly drops for cell- and bead concentrations exceeding four million per milliliter hydrogel. In addition, hydrogels with high cell concentrations ($\geq$6 mio ml^{-1}) show more pronounced material nonlinearity for larger strains and faster stress relaxation. Our findings highlight cell concentration as a crucial parameter influencing the final hydrogel mechanics, with implications for microgel bead drug carrier-laden hydrogels, biofabrication, and tissue engineering.

1. Introduction

Hydrogels are three-dimensional polymer networks of high water content,[1,2] which have found a wide range of applications in the context of tissue engineering (TE). Synthetic hydrogels such as polyethylene glycol (PEG),[3] 2-hydroxyethyl methacrylate (HEMA)-based hydrogels,[4] poly(oxazoline)s (POx),[5] or polyacrylamide (PAAm), as well as naturally derived hydrogels such as alginate, gelatin, collagen, or fibrin matrices,[6–9] have been used in various biomedical appli-

[a]*Institute of Biomaterials, Department of Materials Science and Engineering, Friedrich-Alexander-University Erlangen-Nürnberg, 91058 Erlangen, Germany. E-mail: thomas.distler@fau.de, aldo.boccaccini@fau.de*
[b]*Institute of Applied Mechanics, Department of Mechanical Engineering, Friedrich-Alexander-University Erlangen-Nürnberg, 91058 Erlangen, Germany. E-mail: silvia.budday@fau.de*
[c]*Institute of Medical Biotechnology, Department of Chemical and Biological Engineering, Friedrich-Alexander-University Erlangen-Nürnberg, 91056 Erlangen, Germany*
[d]*Max Planck Institute for the Science of Light and Max-Planck-Zentrum für Physik und Medizin, Erlangen-Nürnberg, 91058 Erlangen, Germany*
[e]*Chair of Biological Optomechanics, Department of Physics, Friedrich-Alexander-University Erlangen-Nürnberg, 91058 Erlangen, Germany*
†Electronic supplementary information (ESI) available. See DOI: 10.1039/D0BM02117B
‡Equal contributions.

cations.[1] Frequently, these include the delivery of cells,[10–14] growth factors,[15–17] or drugs,[18–22] *in vitro* tissue and tumor models,[23–25] and tissue engineering (TE) matrices.[2,26–30]

The role of biopolymer hydrogels in TE is to chemically and physically mimic the extracellular matrix (ECM) environment to facilitate controlled cell adhesion, proliferation, differentiation, and matrix remodeling.[7,26] Therefore, not only chemical properties of hydrogels such as surface functionality or water absorption capacity play an important role,[1] but also the mechanical characteristics of artificial ECM materials need to be known and tuned according to their intended application.[31–35] Previous studies have shown that neural progenitor or pre-osteoblast cells are more likely to adhere, differentiate, and proliferate when the artificial ECM has similar properties to the native ECM.[36,37]

Importantly, the mechanical characteristics of biomaterial hydrogels can be tuned by various means, such as composition,[32,35,38–42] chemical functionalities,[43] microstructure,[44] and cross-linking mechanisms.[45–47] Research on the mechanical properties of materials for TE, therefore, has been frequently focused on a single stiffness value and how it affects cell adhesion, proliferation, and differentiation.[48,49] However, the nonlinear behavior of the native tissue ECM and of many artificial ECM materials requires a more complex mechanical assessment to fully reconstitute nonlinearity and time-dependent mechanical characteristics.[35,50,51]

Despite the fact that advanced scaffold fabrication techniques, such as biofabrication approaches embedding cells inside a 3D-printed hydrogel matrix,[52–62] are a major research focus in TE lately, little is known on how cells incorporated into a material influence the final mechanical properties of the cell–matrix composite.[50,63,64] Consequently, there is a pressing need to understand how cell concentration might affect the mechanical properties of specific hydrogel systems. Interestingly, van Oosten et al.[50] showed that the response of fibrin-based hydrogels to tension is stiffer than that to compression (different from native brain tissue[51]), which was inverted when cells were embedded inside the gels.[50] Hence, cells inside hydrogels can significantly alter the qualitative compression–tension asymmetry behavior, likely to be dependent on the hydrogel system investigated. In addition, cell density and growth combined with ECM production have been shown to alter the mechanical properties of hydrogels during TE construct maturation and represent crucial parameters for successful TE. For instance, human cancer-associated fibroblasts embedded in collagenI/Matrigel™ hydrogels were found to stiffen the material with increasing cell number,[63] which was associated with matrix remodeling caused by the cells inside the matrix during incubation and was overcome by the inhibition of ROCK 1/2 kinases.[63] Significant increases of aggregate and Young's modulus were also found in agarose hydrogels incubated with different cell densities over time.[64] The effect was linked to the increasing glycosaminoglycan (GAG) and collagen content in the ECM, synthesized by the embedded cells.[64]

Mechanical tissue- and organ-substitutes, to be used as, e.g., soft tissue phantoms or surgical models, have been engineered using various hydrogels.[38,50,65–67] We previously found that alginate-based gels without embedded cells can imitate mechanical characteristics of brain tissue.[38] In contrast to fibrin-based hydrogels,[50] the matrix material showed a stiffer behavior for compression than for tension, mimicking the asymmetry found in native brain tissue.[38,51] Yet, matrices different from pristine alginate are required to allow for matrix remodeling, cell proliferation, and hydrogel degradation, to ensure successful TE approaches.[43]

To overcome the limited cell–material interaction and degradation behavior of pristine alginate, advanced alginate-based hydrogels have been introduced,[19,61,68] which include derivatives with increased cell–material interaction through specific integrin binding motifs[28,69–72] and proteins,[31,73,74] combined with a tailored degradation behavior through oxidation of the alginate.[75–78] Aldehyde groups resulting from the oxidation process allow for reversible covalent bonds between the oxidized alginate and amine groups of proteins such as gelatin,[68,79–82] increasing their protein binding capacity and cell adhesion properties.[28] The applicability of oxidized alginate-gelatin (ADA-GEL) hydrogels has been demonstrated in several TE applications,[75] including bioprinting approaches embedding cells.[60,82–87] However, the influence of cells embedded in ADA-GEL hydrogels on the detailed resulting complex mechanical characteristics still remains unknown.

ADA-GEL hydrogels consist of ionically crosslinked oxidized alginate polysaccharide combined with reversibly, covalently bound gelatin, which contrasts with fibrous, network-building collagen or fibrin-based hydrogels, on which the impact of cell-fillers has been investigated before.[50] We have shown in previous studies by second harmonic generation (SHG) imaging that ADA-GEL does not possess highly ordered fibrillar structures,[84,88] hence can be assumed as a non-fibrillar hydrogel. Its non-fibrous crosslinking structure renders ADA-GEL as an excellent candidate to study the effect of cellular fillers on the mechanical properties of non-fibrous hydrogel matrices, especially as this hydrogel proved its potential for TE[75,76] and biofabrication[82,84,85,89,90] applications.

The goal of this work is to investigate the influence of increasing cell density on the mechanical properties of ionically cross-linked ADA-GEL hydrogels. In addition, we aim to evaluate whether PAAm microgel beads can mimic the effect of embedded cells as a filler model system. PAAm microgel beads have shown the potential to mimic cells with respect to their diameter and elasticity, and to allow for a comparison between different mechanical assessment techniques, such as atomic force microscopy (AFM) and real-time deformability cytometry (RT-DC).[91] Due to their mechanical similarities to cells, PAAm beads have been used as stress sensors,[91–93] for the calibration of RT-DC measurements,[94] and to build 3D colloidal scaffolds with spatially differing mechanical layers for cell growth, migration and mechanosensitivity studies.[95] Here, we investigate the mechanical properties of hydrogels containing PAAm microgel beads and embryo mouse fibroblast (NIH/3T3) cells for small and large deformations under compression, tension, and torsional shear loadings. We specifically investigate time-dependent and nonlinear effects to systematically study the influence of different filler concentrations and potential differences between PAAm microgel beads and cells inside the hydrogel matrix. To underpin the mechanical characterization, we assess bead and cell distributions inside the gels using multiphoton microscopy techniques.

2. Materials and methods

2.1. Oxidized alginate synthesis

Sodium alginate (PH 176, VIVAPHARM alginate, JRS PHARMA GmbH & Co. KG, Rosenberg, Germany) was oxidized following an adapted protocol of controlled oxidization as described previously.[78] In brief, sodium alginate (10 g) was oxidized using 9.375 mmol sodium metaperiodate (Sigma Aldrich, Germany) in 100 ml of a water–ethanol (50 : 50 v/v) for 6 hours in the absence of light. The oxidation reaction was quenched using 10 ml of ethylene-glycol (Sigma Aldrich, Germany) and the solution was dialyzed against ultrapure water (UPW, Type II, MilliQ) using dialysis tubes (Molecular Weight Cut-off (MWCO): 6–8 kDa, Spectra/Por, Spectrum Laboratories, US) for three days. The water was changed daily to ensure the complete extraction of the oxidant, ethanol, and reaction byproducts. The oxidized alginate (alginate dialdehyde, ADA) was

frozen overnight and lyophilized for 72 h to yield a dry product.

2.2. Hydrogel formulation

Hydrogel precursor solution was obtained by dissolving 7.5% (w/v) ADA in Dulbecco's phosphate-buffered saline (DPBS, Gibco, Germany) and 7.5% (w/v) gelatin (GEL) (Typ A, from porcine skin, Bloom 300, Sigma Aldrich, USA) in UPW under continuous stirring at 37 °C. Both solutions were passed through 0.45 m (ADA) and 0.22 m (GEL) syringe filters (Rotilabo®, Carl Roth GmbH & Co. KG, Germany), respectively. ADA and GEL were mixed in a 1 : 1 ratio and stirred until a homogeneous solution with a final concentration of 3.75%/ 3.75% (w/v) ADA-GEL was obtained.

2.3. Cell culture and maintenance

To assess the influence of cells on the mechanical properties of hydrogel samples, NIH/3T3 cells (passage P7-P28) (murine embryo fibroblasts 3T3, ATCC® CRL-1658™, ATCC, USA) were used. The cells were cultured using a high glucose Dulbecco's Modified Eagle's Medium (DMEM, Gibco, Germany), supplemented with bovine calf serum, L-glutamine, sodium pyruvate and penicillin–streptomycin (Gibco, Germany), at 37 °C under a controlled humidified atmosphere (98% air, 5% CO_2) in an incubator. Cells were passaged by washing with DPBS and detaching using 0.25% Trypsin/EDTA (Gibco, Germany).

2.4. Preparation of polyacrylamide microgel beads

PAAm beads were produced as described previously.[91] Briefly, a polydimethylsiloxane (PDMS)-based flow-focusing microfluidics device interfaced with a pressure-based microfluidics controller (Fluigent MFCS-EX) was used to produce pre-gel monodisperse droplets in oil (Fig. 1a). The pre-gel mixture was obtained by dissolving acrylamide (7.6% w/v), bis-acrylamide (0.2% w/v) and ammonium persulphate (0.8% w/v) in 10 mM

TRIS buffer (all Sigma Aldrich, Germany). The oil (HFE-7500, 3M™, USA) solution was prepared by dissolving ammonium Krytox surfactant (1.5% w/w), TEMED (0.4% v/v) and N-hydroxysuccinimide ester (NHS, 0.1% w/v), (Sigma Aldrich, Germany). After production, the droplets dispersed in the oil solution were incubated overnight at 65 °C to complete the polymerization. Finally, the beads were washed three times by centrifugation and resuspended in 1× PBS. To functionalize the beads with Alexa Fluor™ 488 Hydrazide (Thermo Fisher Scientific, USA), the beads were re-suspended in 50 mM HEPES (Carl Roth, Germany) dissolved in UPW. After incubation overnight, the functionalized PAAm microgel beads were washed three times with 1× PBS and stored at 4 °C until further use.

2.5. Sample preparation

To study the influence of embedded cells and PAAm microgel beads on the mechanical behavior of ADA-GEL hydrogels, we chose different filler densities between 1 million fillers per ml and 8 million fillers per ml, as summarized in Table 1. Table 1 additionally reports the number of specimens and the corresponding passages of NIH/3T3 cells for the different test series. Cells were counted using the Trypan blue (Gibco, Germany) exclusion method with a Neubauer counting chamber (Paul Marienfeld GmbH & Co. KG, Germany). The cells were centrifuged and then dispersed in the hydrogel precursor solution after carefully removing the cell medium. PAAm microgel beads were treated analogously, except for the use of Trypan blue.

We fabricated ADA-GEL cylinders using a custom-designed platinum-catalyzed silicone model (Ecoflex™ 00-50, Smooth-On Inc., USA). The mold negative for the casting of ten cylinders (d = 8 mm, h = 4 mm) was first fabricated from polylactic acid (PLA) using a polymer 3D-printer (Ultimaker 2+, Ultimaker, Netherlands). Next, the silicone mold was placed in Petri dishes (d = 92 mm, Sarstedt, Germany) and 200 l of hydrogel precursor solution were pipetted into each mold. The solution was carefully spread to the edges of the mold to allow for a flat specimen surface and to avoid bubbles. The hydrogels were left to set for 20 min to allow partial gelatin solidification, followed by crosslinking using 0.1 M $CaCl_2$. After five minutes, the mold was removed after detaching the specimens by using a spatula. The samples were allowed to additionally crosslink for five minutes before detaching them with the spatula from the Petri dish. Afterwards, the samples were cross-linked for another 35 minutes, so that a total cross-linking time of 45 minutes was reached. An exemplary cross-linked ADA-GEL sample is illustrated in Fig. 2a. We finally transferred the samples into DMEM, which was chosen as the storing and testing medium for the mechanical analyses.

2.6. Experimental setup

For the mechanical measurements, a Discovery HR-3 rheometer (TA Instruments, New Castle, USA) was used. To maximize adhesion between the specimens and the geometry of the rheometer, sandpaper was attached to the upper and lower
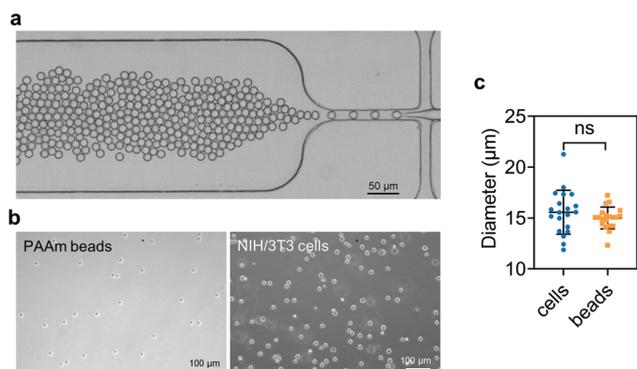

Fig. 1 PAAm microgel beads and mouse NIH embryo-fibroblast (NIH/3T3) cells used as fillers in this study. (a) Microfluidics chip device used for the production of pre-gel bead droplets. (b) Light microscopy images of PAAm beads and NIH/3T3 cells after trypsinization. (c) Sphere diameter of PAAm beads and NIH/3T3 cells (n = 20). Data are shown as mean ± SD. Microgel beads and cells of similar diameters were used (Welch's t-test).

Table 1 Cell and PAAm microgel bead concentrations used in ADA-GEL hydrogels

Study		Pure ADA-GEL	1 million per ml	2 million per ml	4 million per ml	6 million per ml	8 million per ml
Beads	No. of samples	$n = 5$	$n = 5$	$n = 5$	$n = 5$	—	$n = 6$
Cells	No. of samples	$n = 5$	$n = 5$	$n = 5$	$n = 5$	$n = 5$	$n = 5$
	Cell passage	—	P7	P12	P15	P28	P24
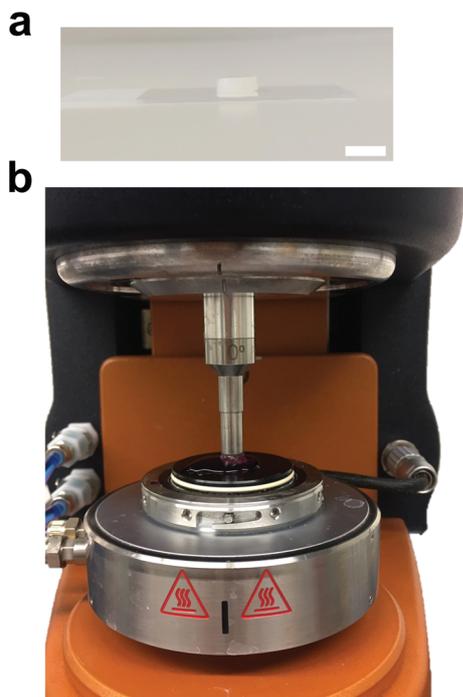
Fig. 2 Experimental setup. (a) Ionically Ca^{2+} cross-linked ADA-GEL hydrogel sample. Scale bar: 10 mm (b) testing setup with sample mounted to the rheometer and surrounded by cell culture medium (DMEM) to avoid dehydration.

Table 2 Testing protocol for the mechanical analysis of cell- and PAAm microgel bead-laden hydrogel specimens

Loading condition	Max. strain	Loading rate
Frequency sweep	1%	0.1–10 Hz
Cyclic compression and tension	15%	40 m s^{-1}
Compression stress relaxation	15%	Undefined
Tension stress relaxation	15%	Undefined
Cyclic shear	15%	0.3333 rad s^{-1}
Cyclic shear	30%	0.1667 rad s^{-1}
Shear stress relaxation	30%	0.1 s (rise time)

by DMEM at all times. The protocol started with a frequency sweep from 0.1 to 10 Hz at a maximum shear strain of 1% to quantify the small-strain behavior of the hydrogels. Subsequently, cyclic compression–tension experiments with a maximum strain of 15% and a loading velocity of 40 m s^{-1} were performed, followed by stress relaxation experiments at a maximum strain of 15% and a holding time of 300 s each. Finally, two sets of cyclic shear experiments were performed with maximum strains of 15% and 30%, and an angular frequency of 0.3333 rad s^{-1} and 0.1667 rad s^{-1}, respectively, followed by a shear stress relaxation test at 30% maximum shear strain (reached within 1 s) with a holding time of 300 s. After mechanical testing, the ADA-GEL samples were carefully removed from the geometries by using a scalpel and stored in DMEM for subsequent microstructural investigations.

2.7. Analysis of filler distribution

To analyze the distribution of cells inside the ADA-GEL hydrogels, cell-laden samples were stained for cell nuclei using 1 l ml^{-1} Hoechst 33342 (Hoechst 33342, H3570, Invitrogen™, Germany) solution (in HBSS) for 40 minutes in the absence of light. The specimens were washed with Hank's Balanced Salt Solution (HBSS, Sigma Aldrich, Germany) and fixed using 4% formaldehyde (Sigma Aldrich, Germany) for 20 minutes. All samples were stored in HBSS at 4 °C before imaging.

2.8. Multiphoton microscopy

The distribution of cells and beads inside ADA-GEL hydrogels was analyzed using a multiphoton microscope (TriMScope II, LaVision BioTec, Bielefeld, Germany). Hoechst stained cells were excited using a modelocked ps-pulsed Ti:Sa laser (Chameleon Vision II, Coherent, Santa Clara, USA) at 810 nm wavelength. The cell-sample's fluorescence was recorded using a 450/30 nm single bandpass filter (Chroma Technology group, Acal BFi Germany GmbH, Germany) and a non-des-

specimen holder before mounting the samples by using instant glue (Cyanacrylat, Henkel AG & Co. KGaA, Germany), as described in ref. 38. Before starting the testing protocol, an axial force of 0.03 N was applied to ensure contact between the geometry and the specimen. As the samples were fixed for microstructural analyses after mechanical testing, we refrained from testing the samples immersed in fluid. Instead, we carefully hydrated the specimens with DMEM, as illustrated in Fig. 2b. All mechanical measurements were performed at room temperature (22 °C, RT), as hydrogel degradation may have affected the results at elevated temperatures.[78] When testing fluorescent PAAm microgel bead-laden ADA-GEL samples, the setup was covered using a black cardboard to avoid photobleaching.

The testing protocol combined different loading conditions, loading modes (compression, tension, torsional shear), strains, and strain rates to appropriately characterize both the small- and large-strain response of these nonlinear and viscoelastic materials, as summarized in Table 2. Each sample was measured for ~25 minutes, keeping the hydrogel surrounded

canned transmission photomultiplier tube (PMT). The Alexa488-conjugated bead fluorescence was recorded using a 525/50 nm (Chroma Technology group, Acal BFi Germany GmbH, Germany) single bandpass filter and the same PMT. A 25× HC FLUOTAR L objective (Leica Microsystems GmbH, Germany) was used throughout the imaging. Voxel sizes of 0.4 × 0.4 × 1 m³ in images with a field of view of 400 m² were recorded, maintaining pixel counts of 512 × 512 pixels (X–Y) and 1292 pixels (Z).

2.9. Image analysis

All images were processed using Fiji (NIH).[96] For image quantification, image volumes of 0.4 × 0.4 × 1 mm³ were recorded. The nearest neighbour distance d_{min} among cells and beads was calculated from 3D reconstructions of the imaged volumes using Matlab (MathWorks Inc, US), and was defined as the smallest distance among all proximate neighbours ($N > 294$) of each individual filler inside the hydrogel volume. The number of fillers was quantified from three individual volumes per concentration. The mean nearest neighbour distance was calculated for each individual volume ($n = 3$) per concentration.

2.10. Real-time deformability cytometry (RT-DC)

Cell and bead elasticity were assessed using RT-DC, as described previously.[91,97] Briefly, NIH/3T3 cells and PAAm beads were suspended in MC 0.5% (w/v) in 1× PBS (3 × 10⁶ ml⁻¹) and flow-focused in a 30 m narrow square channel, applying a total flow rate of 0.12 and 0.24 l s⁻¹, respectively. The flow rate was adapted to account for sufficient deformation inside the narrow channel, in the range of 0.005–0.05 for further calculation of the Young's modulus. The cell and bead deformation *vs.* size was analyzed in real-time and a method based on numerical simulations was used to calculate their Young's modulus.[98] The deformation d is defined by the following equation[97]

$$d = 1 - c = \frac{2\sqrt{\pi A}}{l} \tag{1}$$

where c is the circularity of the cell/bead, A is the projected area, and l is the perimeter of the cell/bead.

2.11. Data analysis and material modeling

To describe the macroscopic deformation of each tested specimen, we used the nonlinear equations of continuum mechanics and introduced the deformation map $\boldsymbol{\varphi}(\mathbf{X},t)$, which maps tissue from the undeformed, unloaded configuration to the deformed, loaded configuration.[99] The deformation gradient $\mathbf{F}(\mathbf{X},t) = \nabla_{\mathbf{X}}\boldsymbol{\varphi}(\mathbf{X},t)$ maps line elements in the undeformed sample to the corresponding line elements in the deformed sample, where $\mathbf{X}$ and $\mathbf{x}$ denote the position vectors in the unloaded and loaded configurations, respectively. The principal stretches λ_i, $i = 1, 2, 3$, are the square roots of the eigenvalues of the left and right Cauchy Green tensors defined by $\mathbf{b} = \mathbf{F}\mathbf{F}^T$ and $\mathbf{C} = \mathbf{F}^T\mathbf{F}$, where $[\mathbf{F}] = \text{diag}\{\lambda_1,\lambda_2,\lambda_3\}$. We assumed that the samples deformed homogeneously in compression

and that the filled ADA-GEL hydrogels are incompressible due to their high water content, characterized by det $\mathbf{F} = 1$.

In uniaxial compression and tension, we computed the stretch as $\lambda = 1 + \Delta z/H$, with specimen height H and z-displacement Δz. The corresponding Piola stress P_{zz} was calculated as the measured force f_z divided by the cross-sectional area A of the specimen in the unloaded reference configuration, *i.e.* $P_{zz} = f_z/A$. Under the assumption of uniform deformation and for unconfined lateral surfaces, the deformation gradient $\mathbf{F}$ yields

$$[\mathbf{F}] = \begin{bmatrix} 1/\sqrt{\lambda} & 0 & 0 \\ 0 & 1/\sqrt{\lambda} & 0 \\ 0 & 0 & \lambda \end{bmatrix}, \tag{2}$$

with the principal stretches

$$\lambda_1 = \lambda_2 = \frac{1}{\sqrt{\lambda}} \quad \text{and} \quad \lambda_3 = \lambda. \tag{3}$$

We model the compression–tension response of the samples by considering the modified one-term Ogden model strain-energy function for a hyperelastic, incompressible material $\Psi = \frac{2\mu}{\alpha^2}\left(\lambda_1^\alpha + \lambda_2^\alpha + \lambda_3^\alpha - 3\right)$, where α denotes the nonlinearity parameter and μ the classical shear modulus.[51,100] We can then express the Piola stress tensor $\mathbf{P}^\Psi$ as the derivative of the strain-energy function Ψ with respect to the deformation gradient $\mathbf{F}$.[99] For an incompressible hyperelastic material with det $\mathbf{F} = 1$, we obtain

$$\mathbf{P}^\Psi = \frac{\partial \Psi}{\partial \mathbf{F}} - p\mathbf{F}^{-T} = \sum_{i=1}^{3} \frac{\partial \Psi}{\partial \lambda_i}\mathbf{n}_i \otimes \mathbf{N}_i - p\mathbf{F}^{-T} \quad \text{with} \tag{4}$$

$$\frac{\partial \Psi}{\partial \lambda_i} = 2\mu\lambda_i^{\alpha-1}/\alpha \tag{5}$$

where $\mathbf{n}_i$ and $\mathbf{N}_i$ are the eigenvectors of the left and right Cauchy Green strain tensors, respectively, and p serves as a Lagrange multiplier. We determined p by evaluating the condition $P_{xx} = P_{yy} = 0$.

To calibrate the shear modulus μ and nonlinearity parameter α, we used the nonlinear least-squares algorithm *lsqnonlin* in MATLAB and minimized the objective function

$$\chi^2 = \sum_{i=1}^{n}(P_{zz} - P_{zz}^\Psi)_i^2, \tag{6}$$

where n is the number of considered experimental data points, and P_{zz} and P_{zz}^Ψ are the experimentally determined and model predicted Piola stresses, respectively.

To evaluate the 'goodness of fit', we determined the coefficient of determination $R^2 = 1 - S^{res}/S^{tot}$, where $S^{res} = \sum_{i=1}^{n}(P_i - P_i^\Psi)^2$ is the sum of squares of residuals with the experimental data values P_i, the corresponding model data values P_i^Ψ, and the number of data points n, and $S^{tot} = \sum_{i=1}^{n}(P_i - \bar{P})^2$ is

the total sum of squares with the mean of the experimental data $\bar{P} = 1/n \sum_{i=1}^{n} P_i$.

2.12. Statistical analysis

All statistical analyses were performed using either the Statistics Toolbox in MATLAB® (MathWorks, US) or GraphPad Prism software (GraphPad Software, US). A p-value lower than 0.05 was considered to be significant. Multi-comparison tests with separate Tukey-Kramer tests were performed between the different bead and cell concentrations. We evaluated maximum stresses in compression, tension, and torsional shear, as well as the compression–tension asymmetry, Young's modulus, and the nonlinearity parameter α. Comparisons between two groups were performed using Student's or Welch's t-tests (normally distributed) or Mann-Whitney U tests (non-parametric). Statistically significant differences among mean ranks (nearest neighbour distance analysis) were tested

for non-parametric Kruskal-Wallis test with Dunn's multiple comparisons *post-hoc* test.

3. Results

3.1. Imaging

We embedded cells and beads at different filler concentrations inside ADA-GEL hydrogels and assessed the distribution of the fillers using multiphoton microscopy (Fig. 3a). An intact, spherical cell-shape was confirmed without indication of fragmented or spread cells in the autofluorescence channel. Increasing the filler density of cells (blue, Hoechst) and beads (orange colored, AF488) led to a decrease in the distance between neighbouring fillers (Fig. 3a–c). From the multiphoton microscopy data, we reconstructed the 3D filler distribution inside the hydrogels (Fig. 3b) and calculated the nearest distance between two individual neighbouring cells and beads in 3D from the reconstructions (Fig. 3c). The mean
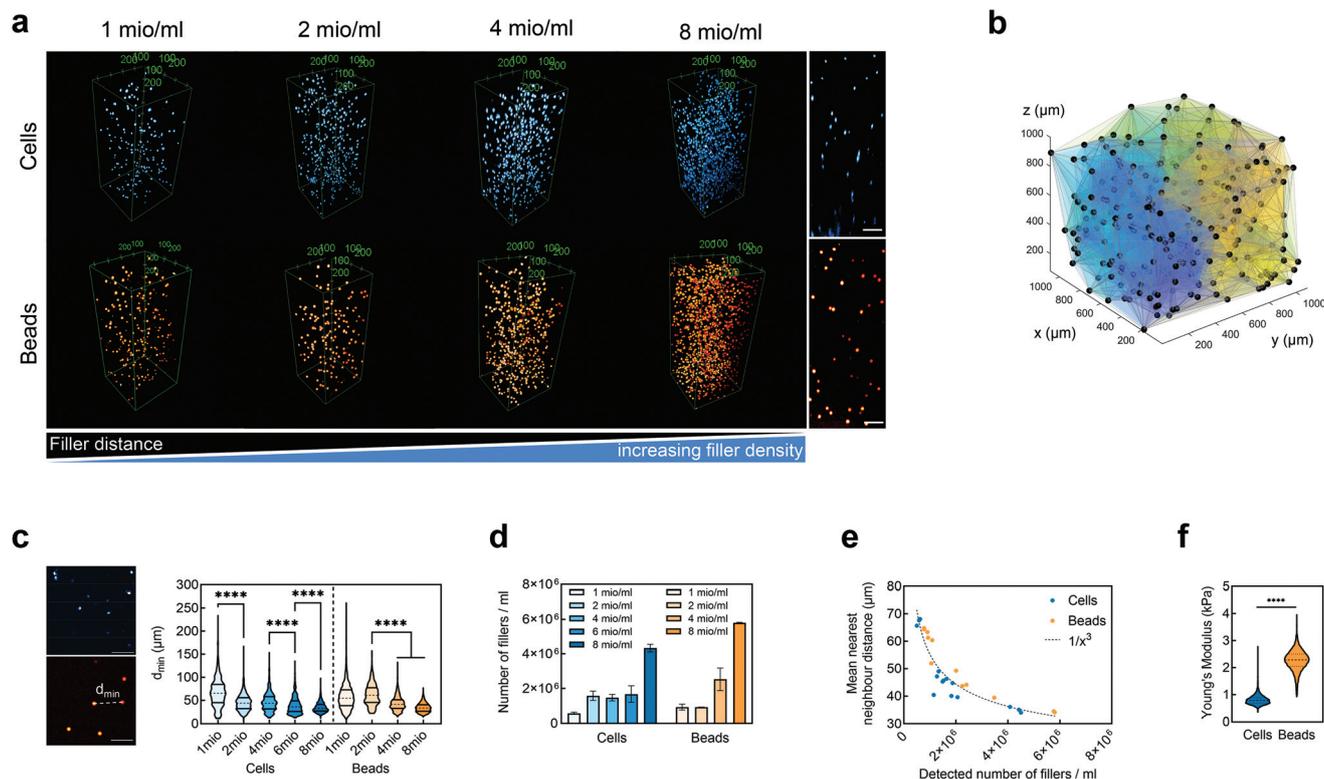
Fig. 3 Cell and bead distribution inside the ADA-GEL hydrogel. (a) Qualitative multiphoton microscopy images of cells and beads inside ADA-GEL hydrogels at filler concentrations of 1, 2, 4, and 8 million per ml. A decrease in mean distance between the fillers with increasing filler density is visible. (right) x–z crossection (8 mio ml^{-1}), scale bars: 100 μm. (b) 3D reconstruction of 2 mio ml^{-1} cell-distribution (black dots) inside the hydrogel used for minimal neighbour distance quantification in 3D. (c) Minimal neighbour distance between nearest neighbours of fillers (cells, beads) inside the hydrogels ($n = 3$) measured as the closest distance between two neighbouring fillers (d_{min}). Data are shown as median (dashed line) and upper/lower 25th/75th percentiles (horizontal lines). Significant differences between mean ranks were analysed using non-parametric Kruskal-Wallis test with Dunn's multiple comparison test (****$p < 0.0001$). (d) Detected number of cells and beads per ml in 1, 2, 4, and 8 million cells per ml (blue) and 1, 2, 4, and 8 million beads per ml (orange) filler density hydrogels. Data are shown as mean $\pm$ SD. (e) Mean nearest neighbour distance as a function of the detected filler density inside the respective hydrogels. (f) Young's modulus of cells and beads ($n > 4500$) determined *via* deformability flow-cytometry. Data are shown as median (dashed line) and upper/lower 25th/75th percentiles (dotted lines). Significant differences between medians of the two groups were analysed using non-parametric Mann-Whitney U test (****$p < 0.0001$).

distance between cells in 1 mio ml^{-1} cell-containing ADA-GEL hydrogels was approx. 67 ± 4 μm. Increasing the cell density from 4 million per ml to 6 and 8 million per ml led to a significantly (****$p < 0.0001$) decreased nearest neighbour distance (Fig. 3c, Videos S1 and S2, ESI†). Increasing the content of beads from 2 million per ml to 4 and 8 million per ml significantly decreased the median nearest neighbour distance from >50 μm to approx. 33 μm (Fig. 3c). The number of fillers detected in the hydrogel showed a noticeable increase from 2, 4, and 6 million cells per ml to 8 million cells per ml (Video S1, ESI†), with similar amounts of cells detected in the 2, 4, and 6 mio ml^{-1} hydrogels (Fig. 3d). For bead-laden hydrogels, an increase in detected bead density was monitored from 2 to 4 million per ml, and 4 to 8 million per ml (Fig. 3c). Plotting the mean nearest neighbour distance as a function of the detected amount of fillers, we observed that the mean neighbour distance decreases at approx. $1/x^3$ with detected number of fillers inside the hydrogels (Fig. 3e). The Young's modulus of the cells was significantly (****$p < 0.0001$) lower in comparison to the polyacrylamide beads (Fig. 3f), as cell stiffness was in the range of 0.6 ± 0.1 kPa and bead stiffness was at 2.2 ± 0.1 kPa, assessed *via* real-time deformability cytometry (Fig. 3f).

3.2. Small-strain behavior of cell- and bead-laden hydrogels

Fig. 4a and b show the storage (G') and loss (G'') moduli for cell- and bead-laden ADA-GEL samples over a frequency range of 0.01 to 10 Hz. In general, G' and G'' are in the same range for both bead- and cell-laden ADA-GEL specimens. Independent of the filler and its concentration, the storage moduli slightly increase with increasing frequency. While bead densities between 2 and 8 million beads per ml in Fig. 4a, left, show similar results to pure ADA-GEL with only a slight decrease in the storage modulus with increasing bead density, the gel with the lowest bead concentration of one million beads per ml exhibits a significantly higher value of G'. However, the theoretical volume fraction of one million beads per ml was approximately 0.2% of the bulk hydrogel (Table 3). Considering the variance of the assessment (Fig. S1, ESI†) and the fact that an increase in G' was solely observed for one million beads per ml but not for further increasing bead concentrations, the data do not allow for a strong conclusion on the observed effect. Concerning cell-laden ADA-GEL hydrogels in Fig. 4a, right, the storage moduli for densities of up to 4 million cells per ml alternate around the results of pure ADA-GEL samples. However, we observe a significant decrease
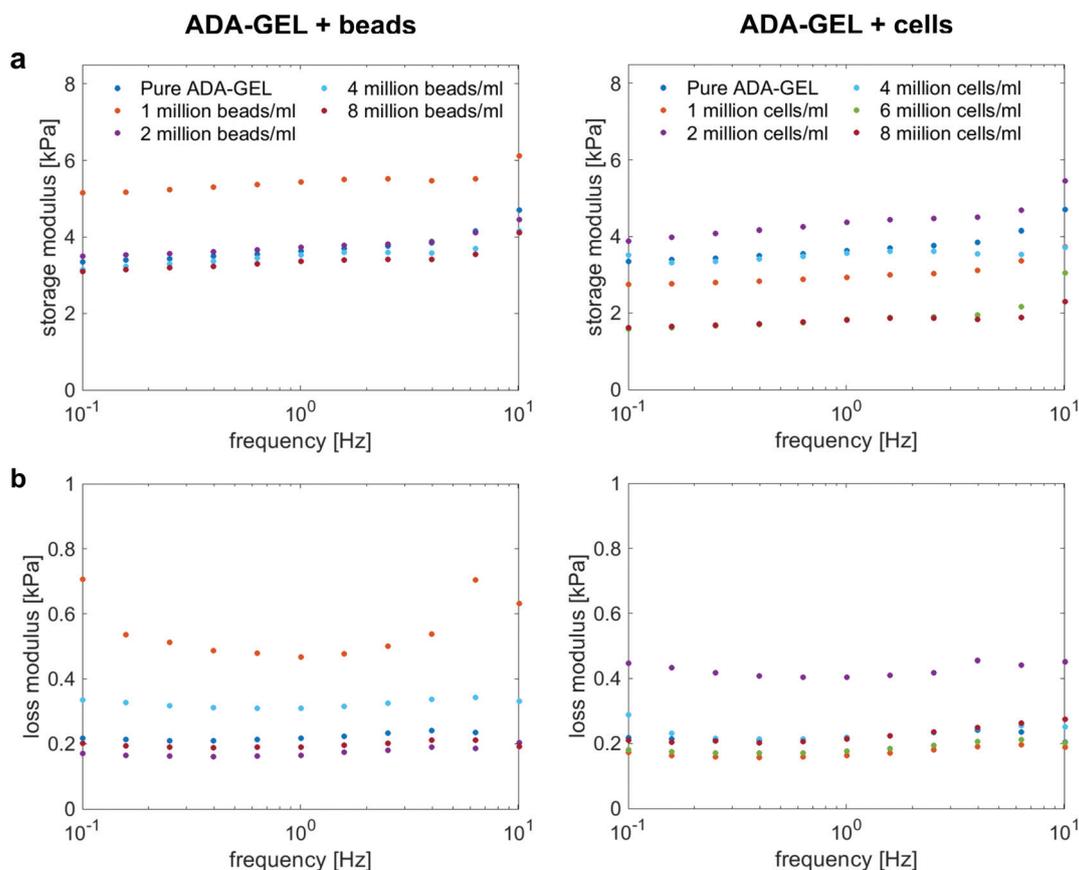

Fig. 4 Storage (a) and loss (b) moduli for ADA-GEL samples with different cell and PAAm microgel bead densities, respectively, at 1% strain over a frequency range from 0.1 Hz to 10 Hz.

Table 3 Theoretical fractional filler volume, Young's moduli E calculated with the model for interaction-free defects, and Young's moduli obtained from fitting the Ogden model to the experimental data for hydrogels containing increasing cell and bead concentrations

| Density (ml^{-1})	Beads			Cells		
	Volume (%)	Analytical E (kPa)	Experimental E (kPa)	Volume (%)	Analytical E (kPa)	Experimental E (kPa)
Pure ADA-GEL	—	—	11.3 ± 0.9	—	—	11.3 ± 0.9
1 million	0.2	11.3	10.8 ± 1.4	0.3	11.3	9.6 ± 1.4
2 million	0.5	11.3	10.8 ± 2.2	0.5	11.3	10.1 ± 1.0
4 million	1.0	11.2	8.6 ± 1.2	1.0	11.2	10.1 ± 1.0
6 million	—	—	—	1.6	11.1	4.0 ± 0.8
8 million	1.9	11.2	9.8 ± 1.0	2.1	11.2	3.5 ± 0.9

in G' when the cell density is increased to 6 or 8 million cells per ml. This may be attributed to the increasing amount (Fig. 3a and d) of softer (Fig. 3f) cells inside the hydrogels, with significantly reduced distance between individual cells (p < 0.0001, Fig. 3c). In general, the effect of cell inclusions on G' is more pronounced than for the inclusions of PAAm microgel beads, especially for high cell concentrations >4 million per ml.

The loss moduli for both bead- and cell-laden hydrogels slightly decrease up to a frequency of approximately 1 Hz, and then slightly increase again for higher frequencies. Similar to the storage moduli of ADA-GEL samples filled with beads, we observe the highest values for samples with a bead density of 1 million per ml, while all other concentrations show similar results to pure ADA-GEL. For cell-laden hydrogel samples, only

the samples with 2 million cells per ml show significantly higher values than the pure ADA-GEL samples, while the data do not indicate a clear correlation between the cell- or bead-filler concentration and the viscoelastic properties of the hydrogels in the small strain (1%) regime (Fig. 4).

3.3. Large-strain behavior of cell- and bead-laden hydrogels

3.3.1. Conditioning behavior. Fig. 5 and 6 show the response of bead- and cell-laden ADA-GEL hydrogels with different filler concentrations during cyclic compression–tension loading with a maximum strain of 15%. Independent of the filler and its concentration, we observe a compression–tension asymmetry with higher stresses for compression than that for tension. In addition, we observe a hysteresis, indicating that energy is dissipated during each loading cycle. This is
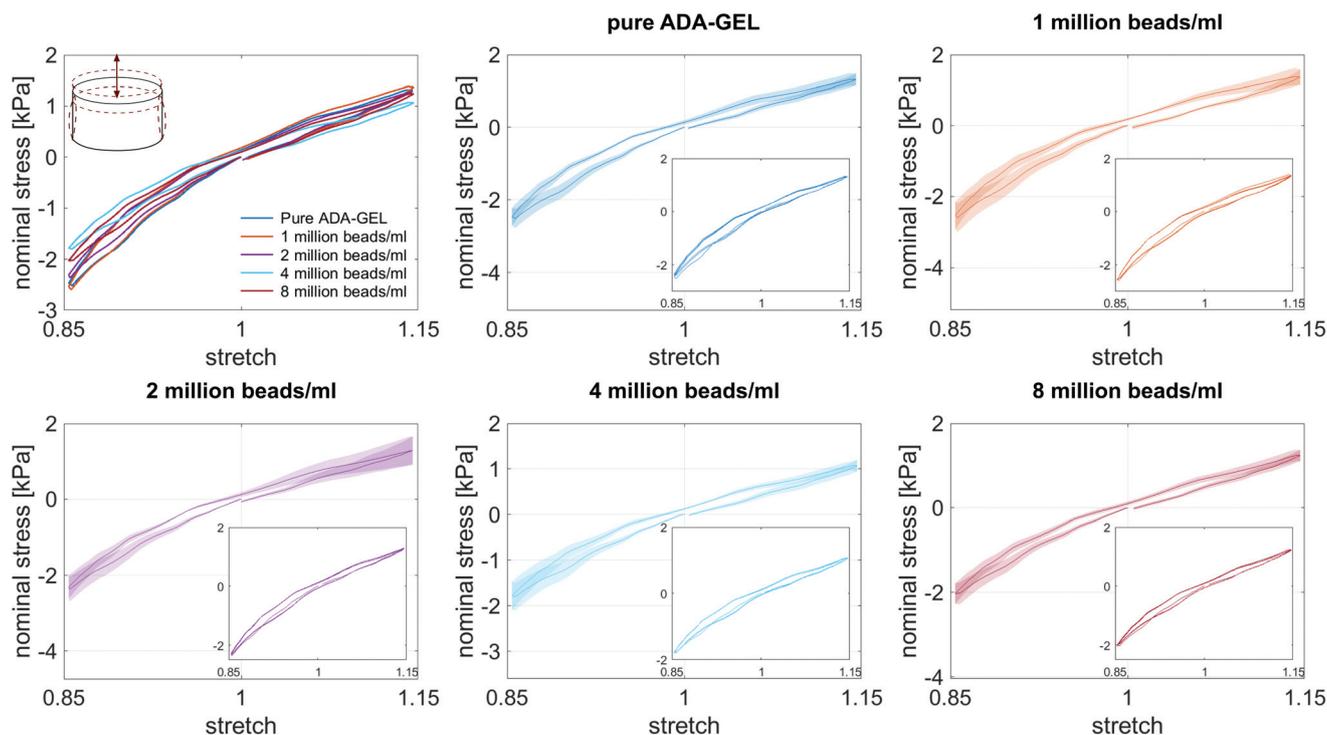
Fig. 5 Response of bead-laden ADA-GEL samples with different bead densities during cyclic compression–tension experiments up to a maximum strain of 15%. The large graphs show the average conditioned response during the third loading cycle with standard deviations, while the small insertions illustrate the conditioning behavior during the whole set of three loading cycles.
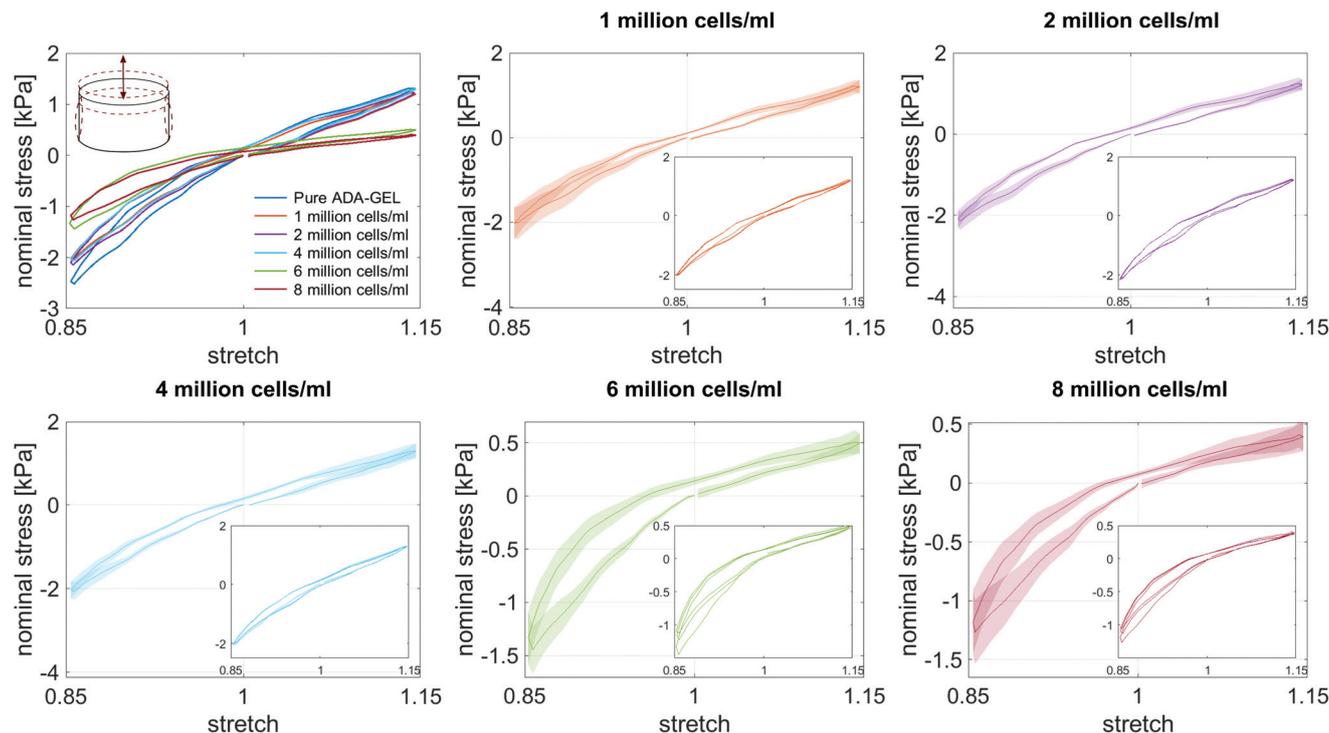
Fig. 6 Response of cell-laden ADA-GEL samples with different cell densities during cyclic compression–tension experiments up to a maximum strain of 15%. The large graphs show the average conditioned response during the third loading cycle with standard deviations, while the small insertions illustrate the conditioning behavior during the whole set of three loading cycles.

especially pronounced for high cell concentrations >4 million per ml. For 6 and 8 million cells per ml hydrogel, the initial loading cycle is characterized by a stiffer and more viscous response than the subsequent cycles (Fig. 6), which might be attributed to the contribution of the softer cell fillers (Fig. 3f) to the stiffer hydrogels, influencing their overall mechanical properties. Importantly, this effect is only visible for cell-laden hydrogels but not for bead-laden hydrogels. Similarly, for shear loadings up to 15% and 30% maximum strains (Fig. S9–S14, ESI†), the addition of >4 million cells per ml results in a softening of the hydrogels after the first loading cycle (Fig. S10 and S12, ESI†), in contrast to the behavior of bead-laden hydrogels (Fig. S9 and S11, ESI†). However, the conditioning between the first and the second loading cycle in shear loading is less pronounced than that for axial loading (Fig. S9–S12, ESI†), highlighting the effect of the loading mode on the observed mechanical response.

Fig. 8 illustrates the average maximum stresses with standard deviations during compressive loading up to 15% strain, tensile loading up to 15% strain, as well as torsional shear loadings up to 15% and 30%, respectively, for bead- and cell-laden hydrogels of different filler densities. In accordance with the observations in Fig. 5 and 6, the maximum nominal stresses are higher for compression than for tension for all hydrogels tested in this work. Regarding hydrogel samples filled with beads, we observe a slight decrease in the maximum stresses for bead densities of 4 and 8 million beads per ml, independent of the loading mode. Furthermore, in shear only,

specimens with 1 and 2 million beads per ml show significantly higher stresses compared to all other concentrations and pure ADA-GEL. Regarding cell-laden hydrogels, the inclusion of lower concentrations (<6 mio ml^{-1}) shows no significant effect on the maximum stresses compared to pure ADA-GEL. However, we observe significantly decreased stresses for all loading modes for higher cell densities of 6 and 8 million cells per ml. The drop in stresses for higher filler densities is much more pronounced for cell- than for bead-laden hydrogels. In both cases, the effect is more apparent in shear than in compression and tension.

3.3.2.   Nonlinearity and material parameters. To quantify the nonlinear, time-independent material response of bead- and cell-laden hydrogels, we determined the shear modulus μ and nonlinearity parameter α by fitting the modified one-term Ogden model to the experimental compression–tension data, as described in subsection 2.11. To this end, we neglect the effects of conditioning and hysteresis and evaluate the average between loading and unloading during the conditioned third loading cycle, as illustrated in Fig. 7 for an exemplary ADA-GEL sample with 2 million beads per ml. The model with only two material parameters is capable of capturing nonlinearity and compression–tension asymmetry, which are the two main time-independent characteristics of the filler-laden hydrogels' mechanical response, with coefficients of determination $R^2 > 0.99$. In the linear elastic limit, the Young's modulus may be calculated as a function of the classical shear modulus and the Poisson's ratio ν, $E = 2\mu(1 + \nu)$. Under the
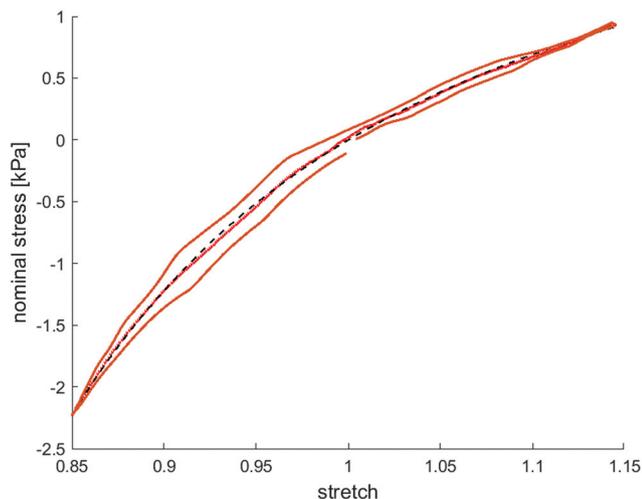
Fig. 7 Calibration of modified one-term Ogden model (black dashed line) by using the average response between loading and unloading (red solid line) to determine time-independent material parameters, shear modulus μ and nonlinearity parameter α, exemplary shown for a ADA-GEL sample with 2 million beads per ml.

assumption of incompressibility with $\nu = 0.5$, we obtain $E = 3\mu$, as reported in Table 3.

Fig. 9 compares the compression–tension asymmetry (**a**), the Young's modulus (**b**) and the nonlinearity parameter α (**c**) for bead- and cell-laden hydrogels of different filler densities. For most of the hydrogels investigated in this work, the compression–tension asymmetry takes on a value of approximately two, which yields that the compression response is twice as stiff as the response in tension. Only the high-cell-concentration hydrogels with 6 and 8 million cells per ml show a more pronounced asymmetry, where compression is more than three times stiffer than tension.

The Young's modulus significantly decreases for both high-bead- and high-cell-concentrations. Interestingly, the Young's modulus decreases for densities higher than 2 million per ml in bead-laden hydrogels, but only for densities higher than 4 million fillers per ml in cell-laden hydrogels. In accordance with the results from small-strain experiments, the drop in the Young's modulus is much more pronounced for the cell-laden hydrogels than for the bead-laden gels.

The drop in stiffness for higher filler concentrations is significantly higher than one would expect considering the low volume fractions of fillers, which hardly exceed 2% (Table 3), even for the highest concentrations of 8 million fillers per ml.
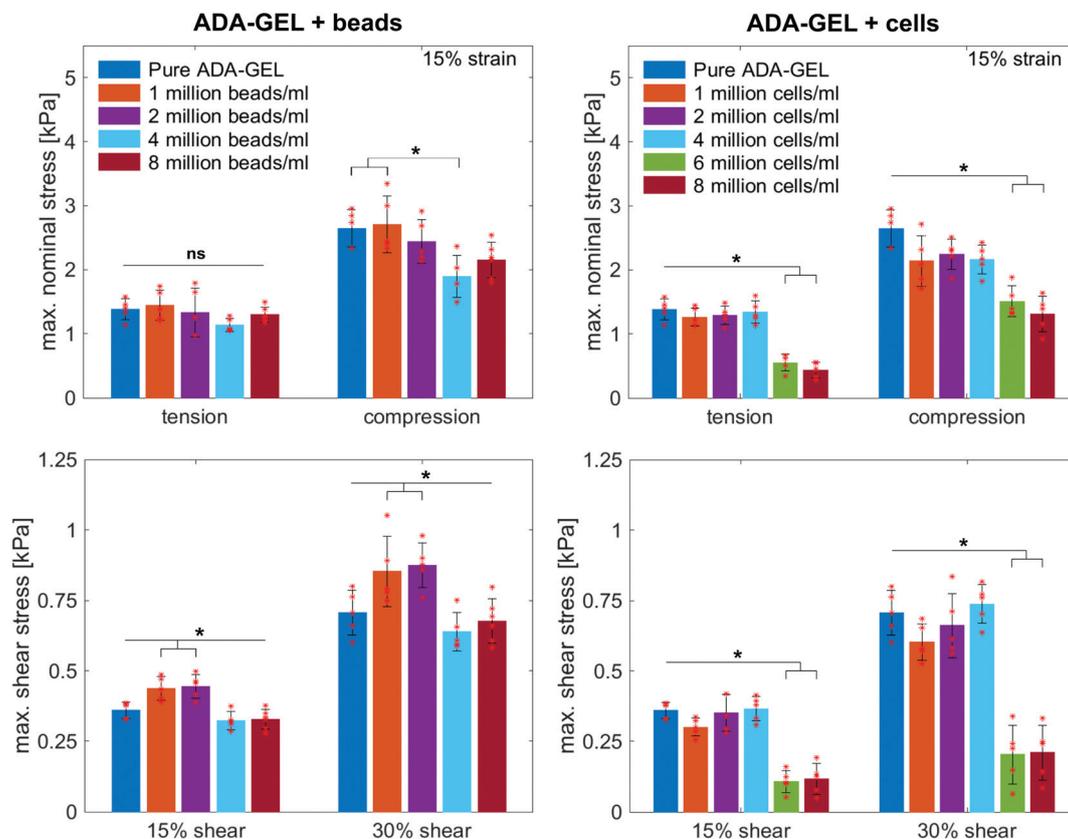
Fig. 8 Average maximum stresses with standard deviations during cyclic compression, tension, and torsional shear experiments for bead- and cell-laden ADA-GEL samples with different filler densities. Asterisks denote statistical significance analysed via one-way ANOVA followed by Tukey–Kramer tests for multiple comparisons (*$p < 0.05$).
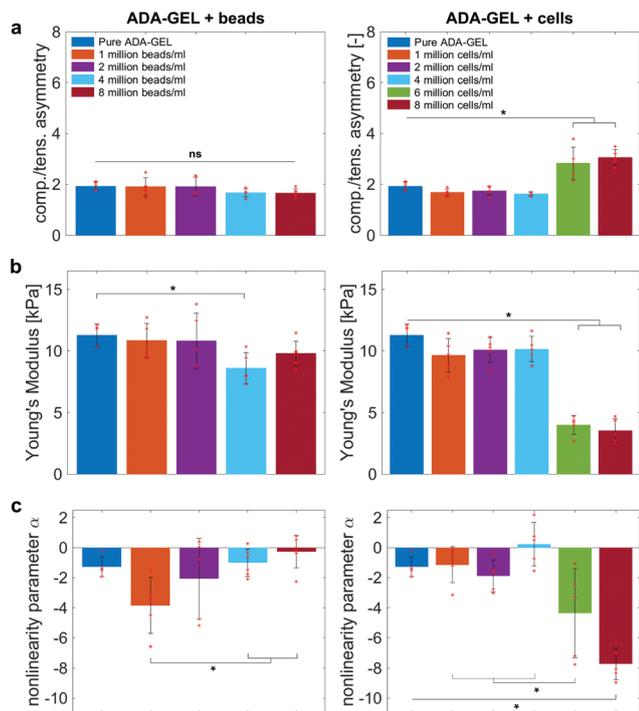
Fig. 9 Average compression–tension asymmetry (a), Young's modulus (b), and non-linearity parameter α (c) with standard deviations for bead- and cell-laden ADA-GEL samples with different filler densities. Asterisks denote statistical significance analysed *via* one-way ANOVA followed by Tukey–Kramer tests for multiple comparisons (*$p < 0.05$).

A first analytical approximation for the effective stiffness of a matrix filled with a low volume fraction of linear elastic, spherical particles may be obtained using the following model for interaction-free defects,

$$\mu_{\text{eff}} = \mu_{\text{m}} + c_{\text{f}} \frac{[\mu_{\text{f}} - \mu_{\text{m}}]}{\mu_{\text{m}} + \beta[\mu_{\text{f}} - \mu_{\text{m}}]} \quad \text{with} \quad \beta = \frac{2[4 - 5\nu]}{15[1 - \nu]}, \quad (7)$$

where μ_{m} and μ_{f} are the shear moduli of the matrix and filler, respectively, and ν is the Poisson's ratio. Due to the incompressibility assumption (see section 2.11), we set $\nu = 0.5$. Table 3 summarizes the estimated volume fractions of fillers, the analytically predicted Young's moduli, and those obtained from fitting the experimental data to the Ogden model. The differences between the theoretically predicted and the experimentally observed stiffnesses are especially high for cell-laden ADA-GEL samples with higher concentrations. While the model predicts a slight decrease in stiffness by approximately 1% for the cell-laden ADA-GEL with highest concentration of 8 million cells per ml, the experiments reveal a drop in stiffness by almost 70%.

The nonlinearity parameter α mostly takes on negative values, which represents the stiffer response in compression than in tension. Values of $\alpha > 2$ would yield the opposite trend. Samples with 1 million beads per ml have a significantly smaller α than samples with 4 and 8 million beads per ml. Again, the cell-laden samples show more significant trends

than the bead-laden hydrogels. The samples with 6 and 8 million cells per ml show a significantly higher nonlinearity than other cell densities and pure ADA-GEL.

3.4. Time-dependent behavior

Fig. 10a shows the average normalized stress relaxation behavior in compression, tension, and torsional shear for bead- and cell-laden ADA-GEL samples of different concentrations. All tested samples did not reach equilibrium within 300 s. In general, the hydrogels relax fastest in tension and reach 3/4 of the initial stress earliest, which is reached latest in shear. Overall, a trend of faster relaxation can be observed with higher filler concentrations. Similar to the results in the previous sections, the hydrogels with high cell concentrations of 6 and 8 million cells per ml show a different behavior in comparison to lower cell concentrations, and relax significantly earlier to 3/4 of the initial stress. The only samples relaxing to a stress value below 50% of the initial stress were cell-laden hydrogels with 6 million cells per ml. Interestingly, those samples ($n = 6$) show a faster relaxation behavior than samples with 8 million cells per ml.

4. Discussion

In this work, we have assessed the complex mechanical response of cell- and PAAm microgel bead-laden hydrogels with different filler concentrations. The mechanical properties of biomaterials play an important role for tissue engineering applications.[8,32] Besides hydrogel degradation,[101] stress relaxation[102,103] especially has proven to be a crucial mechanical parameter that influences cell response. However, often only the mechanical properties of the matrix material are quantified by means of stiffness (Young's modulus) or unimodal viscoelastic (shear) rheological analyses. Only recently, a study on fibrous hydrogel materials has shown that the mechanical properties change through the inclusion of cells, not only quantitatively but also qualitatively.[50]

Here, we have investigated the influence of cell- and PAAm microgel bead fillers on the mechanics of non-fibrous, alginate-gelatin-based hydrogels under compression, tension, and shear.[38] We have combined small-strain and large-strain experiments to assess the distinct nonlinearity, compression–tension asymmetry, and viscoelasticity of this class of materials. This multi-modal mechanical assessment of oxidized alginate-gelatin hydrogels incorporating cells and PAAm microgel bead fillers has important applications for various tissue engineering applications.[10,75,84,85,104]

4.1. High filler concentrations over-proportionally soften the overall material response

The filler stiffness of PAAm microgel beads with an average Young's modulus of 2.2 kPa was significantly higher than the Young's modulus of the NIH/3T3 cells with approx. 0.6 kPa, as found here using RT-DC analysis (Fig. 3f). However, both fillers were significantly softer than the ADA-GEL matrix with a

Young's modulus of approximately 11.3 kPa. For low concentrations, the fillers did not significantly affect the mechanical response neither in the small-strain (Fig. 4) nor in the large-strain regime (Fig. 5–8). This observation was expected as the theoretical volume fraction of the fillers in the hydrogel (ratio of the number of fillers times their volume divided by the total hydrogel volume) was generally very small and never exceeded 2.5%.

However, inclusions of more than 2 million beads per ml or 4 million cells per ml led to a significant drop of stresses for the large-strain loading regime. Comparing the results for maximum shear strains of 15% and 30%, respectively, the drop is more pronounced for higher strains. For cell-containing gels even the small-strain stiffness quantified by the storage modulus during frequency sweeps drops significantly. In general, the stiffness drop is more pronounced for the cell-laden than for bead-laden hydrogels. This effect can be partially attributed to the stiffer response of the beads in comparison to the cells. Still, the inclusion of approximately 1% volume fraction of beads and 1.6% volume fraction of cells leads to a drop in the Young's modulus of 24% and 65%, respectively, which is disproportionally high in comparison to model suggestions of the impact of those filler contents. Therefore, we may conclude that other effects, such as a change of hydrogel cohesion or interference by the fillers in the ionic crosslinking and subsequent hydrogel network formation, affect final hydrogel stiffness. The guluronic acid chain assembly mediated by calcium ions results in the crosslinking of ADA.[78,105] Hence, increasing the amount of fillers may alter the formation of a bulk, homogeneously crosslinked alginate network. The presence of beads and cells may differently decrease the effective crosslinking density in the final hydrogel. The fillers could act as macrostructural heterogeneities affecting the final number of elastic chains in the gel.[106]

The difference in Young's modulus drop could be a result from different interactions of the cells and the beads with the gel network and not only result from the difference of the intrinsic Young's modulus of the cells and beads. Despite the intrinsically higher stiffness of PAAm microgel beads, the approx. 2.5 times smaller stiffness drop of PAAm microgel containing hydrogels may be explained by potential crosslinking reactions between unreacted NHS groups on the PAAm microgel bead surface with ε-amino groups of lysine of gelatin. Together, those effects may counteract the stiffness drop in comparison to the cell-laden gels.

We have demonstrated through multiphoton microscopy techniques that the nearest neighbour distance of fillers inside the hydrogels scaled nonlinearly with increasing filler number (Video S1, ESI†). The mean distance dropped by almost 30% comparing 4 million and 6 million cells per ml. This might explain the sudden drop of stiffness when reaching 6 million cells per ml. The decreased mean filler distance may lead to a disruption in the homogeneous alginate-hydrogel formation in comparison with hydrogels without any spherical fillers. This effect was higher for the cells than for PAAm microgel beads, which can to some extent be attributed to their lower stiffness in comparison to the PAAm microgel beads as well as to the

potential crosslinking of the gelatin with the PAAm microgel bead surface.

The PAAm microgel beads have to be assumed as microporous gel fillers. The pores could be filled by the hydrogel solution and a gelation inside the beads might occur, which cannot happen inside the cells. This may lead to differently hindered crosslinking of the bulk hydrogel due to the different interactions of beads and cells with the gel.

Additionally, cells exhibit a nonlinear elastic behavior and more pronounced viscous effects,[18,107–109] while PAAm beads show an almost elastic response.[91] We expect stress peaks in the matrix in the immediate vicinity of the fillers in the deformed state, preferably in the case of cell-laden hydrogels. The cells in the hydrogels were still in round shape without signs of cell spreading (Fig. 3a), indicating no strongly pronounced cell–material interaction directly after embedding the cells in the hydrogels and crosslinking. As a result, we assume less cell–material interaction with the bulk hydrogel in comparison to the potentially unreacted NHS groups on the functionalized PAAm-bead surface with the hydrogel. This difference to the PAAm beads may ultimately cause the loss of bulk hydrogel stiffness and explain the significant drop in the stiffness observed for cell-laden hydrogels at higher filler concentrations (≥ 6 mio ml^{-1}). As the mechanical properties were assessed directly after embedding the cells in the hydrogels and crosslinking (~45 min), we assume no release of matrix metalloproteinases (MMP) in that time frame, which could cause hydrogel degradation during prolonged *in vitro* cell culture.[80,110–112]

4.2. Hydrogels with high cell concentrations show more pronounced nonlinearity and viscous effects

Along with lower stiffness, the high-cell-concentration hydrogels show more pronounced conditioning during cyclic loading (Fig. 6) in comparison to bead-laden hydrogels (Fig. 5), larger hysteresis, and faster stress relaxation (Fig. 10). We attribute this observation to the nonlinear mechanical properties of the cells[18,107–109] compared to the rather elastic PAAm microgel beads.[91] While we did not observe a clear correlation between filler concentrations and viscous properties for the small strain (1%) regime (Fig. 4), large deformation loadings (15% strain) under multiple loading modes (compression, tension, shear, Fig. 5, 6, Fig. S9–S14, ESI†) revealed that high cell numbers >4 million per ml impact the nonlinearity, compression–tension asymmetry, conditioning behavior, and viscosity of the overall hydrogels, which is in contrast to the behavior observed for bead-laden hydrogels.

Furthermore, we assume that a partial crosslinking of the beads with the hydrogel may explain the higher elastic than viscous response of PAAm bead-laden hydrogels (Fig. 5), and therefore, the less pronounced conditioning behavior and hysteresis. The PAAm beads might be fixed in the matrix due to potential bead–matrix interaction and move together with the matrix during deformation, while the cell movement may be not as synchronized with the matrix deformation due to a lack of interaction. Together with the intrinsic elastic properties of the PAAm microgel beads and the assumed lower interface
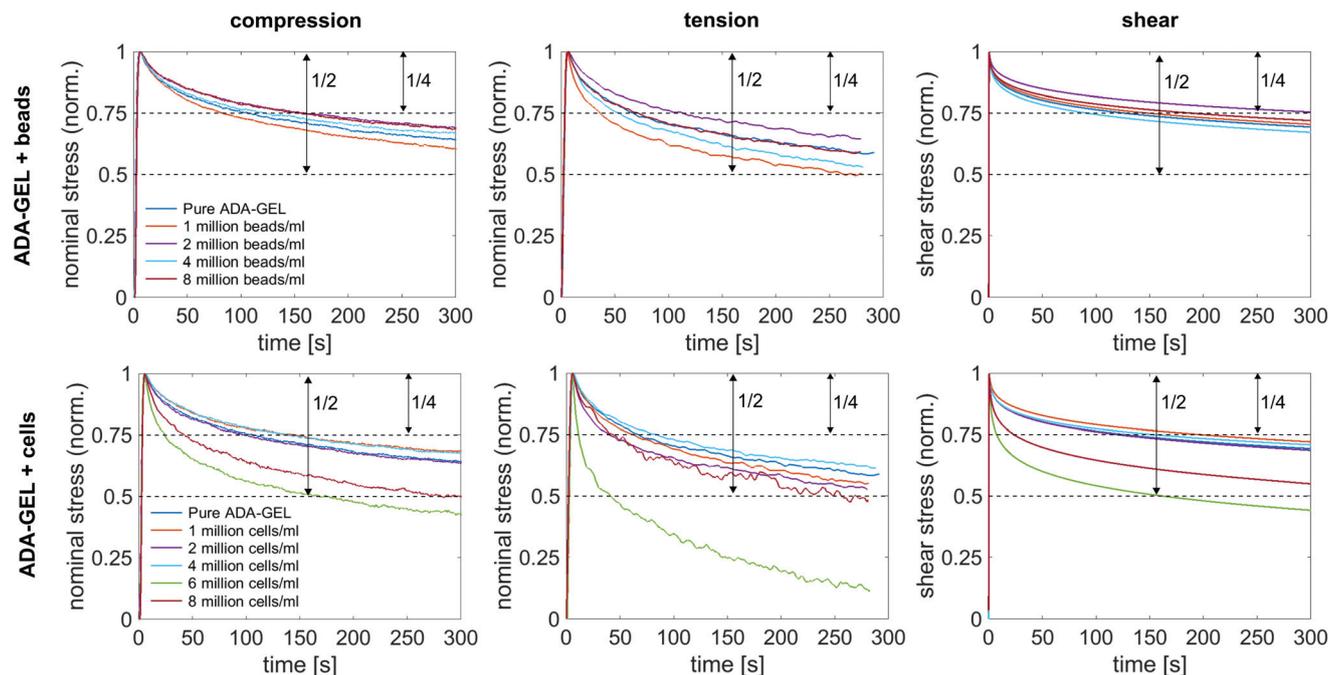
Fig. 10 Stress relaxation behavior of bead- and cell-laden ADA–GEL samples with different filler densities in compression, tension and torsional shear. Time points at which 1/4 and 1/2 of the initial stresses have relaxed are indicated by vertical lines. Data are shown as mean curves from individual samples (n = 5).

interaction of cells with the hydrogel, this may explain the faster relaxation and higher viscous effects observed for the cell-laden hydrogels in compression–tension testing (Fig. 6), especially due to the inherent viscoelastic properties of cells and their cytoskeletal components.[109,113]

The absolute value of the nonlinearity parameter α increases significantly for high cell concentrations. In contrast, it decreases for high bead concentrations. This is in agreement with a recent study showing that cell embedding in fibrous hydrogel networks changed the behavior of the material from compression softening into compression stiffening.[50] In the context of fibrous matrices, this effect was attributed to the alignment of collagenous fibers alongside the volume-conserving cell inclusions, orienting upon compression, and ultimately leading to the stiffening upon compression.[50] The ADA–GEL hydrogels used in this study, in contrast, do not include collagenous fibrous structures, as shown by the absence of second harmonics in comparison to fibrillar collagen type I-based hydrogels.[84,88] Therefore, the effect of hydrogel fiber alignment can be excluded and the main stress-bearing components are the ionic alginate network and the softer cellular inclusions, which leads to a different mechanical response and impact on hydrogel nonlinearity in comparison to fibrous cell-hydrogel systems.[50]

4.3. Cell embedding in biofabrication can alter the final hydrogel mechanics after crosslinking

Biofabrication, which comprises the simultaneous processing of cells and biomaterials to cell-laden constructs, has gained momentum in the past decade.[52,53,58,114] Cell-laden hydrogels, or bioinks, are most commonly used in biofabrication processes.[115] If one considers the relevance of the results obtained in relation to the printing techniques available in biofabrication, extrusion and inkjet printing are particularly relevant. While our results can be transferred primarily to hydrogels produced *via* extrusion printing due to the high viscosity of ADA–GEL (~10^2–10^3 Pa s for low shear-rate regimes <1 s^{-1} (ref. 84)), low-viscosity bioinks are used in ink-jetting (approx. <10^{-2} Pa s,[55] 0.09–0.16 Pa s for ADA–GEL (unpublished data)). Additionally, depending on the geometry of the inkjet needle, very high shear forces can be generated here, which might influence the final cell response in 3D.[116]

As cells are fillers with highly nonlinear mechanical properties,[18,107–109] we found that they can significantly affect the final mechanical properties of the biofabricated construct. This has already been shown in a previous study on fibrous collagen-based hydrogels, which shifted their mechanical properties from compression softening to compression stiffening and thereby, reversed their compression–tension asymmetry by the addition of cells.[50] We show in this study that incorporating cells in non-fibrous oxidized alginate-gelatin-based hydrogels[84] can lead to decreased stiffness, as well as increased compression–tension asymmetry and nonlinearity at cell densities >6 million cells per ml. Cell concentrations of 100 million cells per ml have been utilized for cartilage tissue engineering applications.[102] However, commonly, hydrogel materials are characterized *prior* to the incorporation of cells. As a result, the final mechanical properties of the cell-laden

construct are hardly recapitulated by assessing the hydrogels without cellular filler, especially for high cell numbers. In this study, we have assessed the mechanical properties of cell-laden hydrogels directly after embedding cells inside the gels. The aim was to investigate the influence of cell density on the mechanical properties directly after fabrication, similar to biofabricates. We did not expect cell spreading or morphology changes as fibroblast cells have been shown to proliferate and spread in ADA-GEL only after approximately seven days.[60] This was also confirmed by the spherical cell shape inside the hydrogels observed *via* multiphoton-microscopy analysis, since spread cells would have been visible *via* autofluorescence.[84] Hence, our study provides insights into the influence of spherical cell fillers on the mechanical properties of hydrogels directly after fabrication and cross-linking, and prior to *in vitro* cell culture.

When facing limited resources in terms of limited capabilities to achieve high cell numbers due to, *e.g.*, limited growth capabilities or high costs involved for cell culture, the assessment of the hydrogel mechanics prior to cell addition remains a valid approach. On the other hand, our results indicate that a true understanding of the final hydrogel mechanics with incorporated cells is important and may allow to better recapitulate cell growth, cell proliferation, and maturation in light of the real titab initio biofabricate mechanics (cell-containing-hydrogels), with important implications for future tissue engineering studies and material designs.

4.4. Implications for spherical filler based drug delivery applications and "gel-in-gel" hydrogels

Efforts have been made to engineer polymer microspheres for controlled drug release,[117–120] as well as to incorporate polymer microspheres as drug delivery vesicles into hydrogels.[121–123] Multi-phasic "gel-in-gel" materials have been recently discussed and are currently explored for tissue engineering applications.[124] We used PAAm hydrogel microgel beads with a diameter of approx. 15 μm and stiffness of approx. 2 kPa in this study and show that such fillers can impact the overall mechanical properties of the resulting hydrogel after reaching a threshold concentration. This effect was primarily observed for cells, which have nonlinear mechanical properties. As a result, depending on the hydrogel or polymer material and its intrinsic mechanical nonlinearity, such fillers may influence the complex and time-dependent mechanical properties of the overall hydrogel. In addition, at high concentrations, the mean neighbour distance may influence drug diffusion from the fillers to the hydrogel bulk by changed drug concentration gradients. Regarding tissue engineering, the question arises as to which extent cytokines in the gel can cover a diffusion distance of approx. 30–70 m from cell-to-cell through a defined network density and polymer surface charge provided by the hydrogel.[125–128]

Consideration should also be given to how the degradation rates of the matrix can be adjusted so that the network degrades within a defined time. Ultimately, this can influence controlled tissue development and diffusion.

The altered mechanics of the hydrogel and interaction of hydrogel bulk with the fillers may affect filler degradation and the release of embedded drugs upon deformation. Hence, we suggest to consider the impact of filler concentration and its intrinsic mechanical properties on the final hydrogel mechanics as well as the potential impact of filler-filler distance on drug-release kinetics. Our study further contributed to a better understanding of the potential impact of filler densities on the final hydrogel mechanics of non-fibrous, alginate-based hydrogels.

4.5. Limitations

This study focused on the influence of spherical PAAm microgel beads and cells as fillers on the resulting mechanical properties of oxidized alginate-gelatin hydrogels. The potential interaction of PAAm microgel beads with the hydrogel, specifically with the gelatin component due to the potential presence of unreacted NHS on the bead surface after Alexa Fluor 488™ bead modification, and its potential difference to the cell–material interface, was not comprehensively covered in this study, which we will investigate in future work. We did also not assess bead–material and cell–material interactions in detail. In addition, the deformation of cells and beads inside the hydrogels was not specifically monitored during mechanical deformation. We will assess the *in situ* deformation of cell- and microgel bead fillers during mechanical hydrogel deformation in future work.

During image analysis, we observed that despite the adjustment of the cell concentration between 2, 4, and 6 million cells per ml, similar amounts of cells were detected inside the hydrogel volumes ($n = 3$). The results indicate ambiguity between theoretically counted cell density and the actual amount of cells detected in the hydrogels. However, despite the high penetration depth (1 mm) achieved by the multiphoton microscopy technique, the imaged hydrogel volumes (0.4 × 0.4 × 1 mm^3, 0.16 mm^3, 0.16 μl) only represent a small fraction of the bulk hydrogel sample (approx. 200 mm^3) which was used for mechanical testing. Due to limited resources and imaging time, it was not possible to image volumes in the range of the complete bulk cylinder. This might have caused the difference between imaging and theoretical counting. In addition, counting cells and beads using Neubauer cell counting chambers might have introduced errors leading to discrepancies between the theoretical cell number and measured cell numbers from the imaging volumes. By utilizing automatic cell counters, we will address those potential error sources in the future. Secondly, the amount of imaged hydrogel volume would need to be increased to achieve a total imaged hydrogel volume, which better represents the entire sample.

Despite those challenges, the multiphoton imaging used here allowed us to confirm homogeneous cell and bead distribution inside the imaged volumes, suggesting homogeneous distribution in the bulk samples and an isotropic mechanical response (Fig. 3 and Fig. S10†). Besides the limitation of imaged volume, the technique was confirmed to be highly suit-

Biomaterials Science

able for the assessment of cell- and PAAm microgel bead distribution inside hydrogel specimens beyond penetration depths achieved when using traditional fluorescence imaging techniques.[129]

5. Conclusions

We have demonstrated that low concentrations of NIH/3T3 fibroblast cells and PAAm microgel beads (1–4 mio ml^{-1}) embedded in oxidized alginate-gelatin hydrogels only have a marginal impact on the overall complex mechanical material behavior. However, high cell concentrations ($\geq$6 mio ml^{-1}) inside the hydrogels led to a significant stiffness drop and increased material nonlinearity. This effect was more pronounced for cell than for PAAm microgel bead-laden hydrogels. We show that the inclusion of mechanically nonlinear cells can increase the compression–tension asymmetry of nonfibrous alginate-based hydrogels. Ultimately, the nonlinearity and viscous nature of the cell-containing hydrogels increase in comparison to cell-free hydrogels. The viscous contribution and nonlinearity of cells can, therefore, be a determinant for the final hydrogel bulk mechanics, with important implications towards biofabrication approaches and cell-containing hydrogel designs in tissue engineering.

Author contributions

TD and SB conceptualized the study. TD, RD, and SB developed the methodology. LK performed the main mechanical experiments and data analysis. TD, LK, and SB wrote the first draft. LK, SG, RD, TD, and SB contributed to manuscript writing. TD, DS, and OF conceptualized and performed multiphoton microscopy imaging. DS conducted image data analysis and provided the MATLAB® image analysis code. TD and DS performed imaging data visualization. RG, SG, and JG conceptualized and performed microgel bead fabrication and RT-DC measurements. TD, LK, DS, SG, RG, OF, RD, JG, ARB, and SB contributed to data interpretation and commented on the manuscript. SB and ARB acquired funding and provided resources. SB supervised the overall project. All authors have reviewed and approved the final manuscript.

Conflicts of interest

There are no conflicts to declare.

Acknowledgements

References

1 E. Caló and V. V. Khutoryanskiy, *Eur. Polym. J.*, 2015, **65**, 252–267.

2 J. L. Drury and D. J. Mooney, *Biomaterials*, 2003, **24**, 4337–4351.

3 O. Chaudhuri, L. Gu, D. Klumpers, M. Darnell, S. A. Bencherif, J. C. Weaver, N. Huebsch, H. pyo Lee, E. Lippens, G. N. Duda and D. J. Mooney, *Nat. Mater.*, 2015, **15**, 326–334.

4 O. Wichterle and D. Lim, *Nature*, 1960, **185**, 117–118.

5 J. Blöhbaum, I. Paulus, A.-C. Pöppler, J. Tessmar and J. Groll, *J. Mater. Chem. B*, 2019, **7**, 1782–1794.

6 Y. Li, J. Rodrigues and H. Tomas, *Chem. Soc. Rev.*, 2012, **41**, 2193–2221.

7 N. A. Peppas, J. Z. Hilt, A. Khademhosseini and R. Langer, *Adv. Mater.*, 2006, **18**, 1345–1360.

8 K. Y. Lee and D. J. Mooney, *Chem. Rev.*, 2001, **101**, 1869–1880.

9 A. D. Augst, H. J. Kong and D. J. Mooney, *Macromol. Biosci.*, 2006, **6**, 623–633.

10 B. Balakrishnan and A. Jayakrishnan, *Biomaterials*, 2005, **26**, 3941–3951.

11 Z. Wei, J. Zhao, Y. M. Chen, P. Zhang and Q. Zhang, *Sci. Rep.*, 2016, **6**, 1–12.

12 G. Yang, Z. Xiao, X. Ren, H. Long, H. Qian, K. Ma and Y. Guo, *PeerJ*, 2016, **4**, e2497.

13 S. Duin, K. Schütz, T. Ahlfeld, S. Lehmann, A. Lode, B. Ludwig and M. Gelinsky, *Adv. Healthcare Mater.*, 2019, **8**, 1–14.

14 R. Costa-Almeida, I. Calejo, R. Altieri, R. M. A. Domingues, E. Giordano, R. L. Reis and M. E. Gomes, *Biomed. Mater.*, 2019, **14**, 034104.

15 V. E. Santo, A. M. Frias, M. Carida, R. Cancedda, M. E. Gomes, J. F. Mano and R. L. Reis, *Biomacromolecules*, 2009, **10**, 1392–1401.

16 C. Fu, X. Yang, S. Tan and L. Song, *Sci. Rep.*, 2017, **7**, 1–13.

17 C. R. Silva, P. S. Babo, M. Gulino, L. Costa, J. M. Oliveira, J. Silva-Correia, R. M. Domingues, R. L. Reis and M. E. Gomes, *Acta Biomater.*, 2018, **77**, 155–171.

18 C. W. Yung, W. E. Bentley and T. A. Barbari, *J. Biomed. Mater. Res., Part A*, 2010, **95**, 25–32.

19 K. Y. Lee and D. J. Mooney, *Prog. Polym. Sci.*, 2012, **37**, 106–126.

20 T. Garg, O. Singh, S. Arora and R. S. R. Murthy, *Crit. Rev. Ther. Drug Carrier Syst.*, 2012, **29**, 1–63.

21 M. K. Schesny, M. Monaghan, A. H. Bindermann, D. Freund, M. Seifert, J. A. Eble, S. Vogel, M. P. Gawaz, S. Hinderer and K. Schenke-Layland, *Biomaterials*, 2014, **35**, 7180–7187.

22 C. Elvira, J. F. Mano, J. San Román and R. L. Reis, *Biomaterials*, 2002, **23**, 1955–1966.

23 M. V. Monteiro, V. M. Gaspar, L. P. Ferreira and J. F. Mano, *Biomater. Sci.*, 2020, **8**, 1855–1864.

24 B. Kundu, A. R. Bastos, V. Brancato, M. T. Cerqueira, J. M. Oliveira, V. M. Correlo, R. L. Reis and S. C. Kundu, *ACS Appl. Mater. Interfaces*, 2019, **11**, 14548–14559.

25 R. A. Francescone III, M. Faibish and R. Shao, *J. Visualized Exp.*, 2011, **55**, 2–5.

26 R. Langer and J. P. Vacanti, *Science*, 1993, **260**, 920–926.

27 J. Silva-Correia, J. M. Oliveira, J. S. G. Caridade, R. A. Sousa, J. F. Mano and R. L. Reis, *J. Tissue Eng. Regener. Med.*, 2011, **5**, e97–e107.

28 A. Grigore, B. Sarker, B. Fabry, A. R. Boccaccini and R. Detsch, *Tissue Eng., Part A*, 2014, **20**, 2140–2150.

29 J. Li, C. Wu, P. K. Chu and M. Gelinsky, *Mater. Sci. Eng., R*, 2020, **140**, 100543.

30 B. B. Mendes, M. Gómez-Florit, R. A. Pires, R. M. Domingues, R. L. Reis and M. E. Gomes, *Nanoscale*, 2018, **10**, 17388–17401.

31 G. D. Nicodemus and S. J. Bryant, *Tissue Eng., Part B*, 2008, **14**, 149–165.

32 F. Brandl, F. Sommer and A. Goepferich, *Biomaterials*, 2007, **28**, 134–146.

33 W. F. Liu and C. S. Chen, *Mater. Today*, 2005, **8**, 28–35.

34 K. Franze, P. A. Janmey and J. Guck, *Annu. Rev. Biomed. Eng.*, 2013, **15**, 227–251.

35 M. Jaspers, S. L. Vaessen, P. V. Schayik, D. Voerman, A. E. Rowan and P. H. J. Kouwer, *Nat. Commun.*, 2017, **8**, 1–10.

36 S. K. Seidlits, Z. Z. Khaing, R. R. Petersen, J. D. Nickels, J. E. Vanscoy, J. B. Shear and C. E. Schmidt, *Biomaterials*, 2010, **31**, 3930–3940.

37 C. B. Khatiwala, S. R. Peyton and A. J. Putnam, *Am. J. Physiol.: Cell Physiol.*, 2006, **290**, C1640–C1650.

38 T. Distler, E. Schaller, P. Steinmann, A. R. Boccaccini and S. Budday, *J. Mech. Behav. Biomed. Mater.*, 2020, **111**, 103979.

39 L.-S. Wang, J. E. Chung, P. P.-Y. Chan and M. Kurisawa, *Biomaterials*, 2010, **31**, 1148–1157.

40 J. W. Nichol, S. T. Koshy, H. Bae, C. M. Hwang, S. Yamanlar and A. Khademhosseini, *Biomaterials*, 2010, **31**, 5536–5544.

41 C. Cha, S. R. Shin, X. Gao, N. Annabi, M. R. Dokmeci and X. Tang, *Small*, 2014, **10**, 514–523.

42 L. A. Sawicki and A. M. Kloxin, *Biomater. Sci.*, 2014, **2**, 1612–1626.

43 X. Li, Q. Sun, Q. Li, N. Kawazoe and G. Chen, *Front. Chem.*, 2018, **6**, 1–20.

44 N. Annabi, J. W. Nichol, X. Zhong, C. Ji, S. Koshy, A. Khademhosseini and F. Dehghani, *Tissue Eng., Part B*, 2010, **16**, 371–383.

45 X. Zhao, N. Huebsch, D. J. Mooney and Z. Suo, *J. Appl. Phys.*, 2010, **107**, 1–5.

46 P. M. Kharkar, K. L. Kiick and A. M. Kloxin, *Chem. Soc. Rev.*, 2013, **42**, 7335–7372.

47 S. A. Bencherif, A. Srinivasan, F. Horkay, J. O. Hollinger, K. Matyjaszewski and N. R. Washburn, *Biomaterials*, 2008, **29**, 1739–1749.

48 J. W. Gunn, S. D. Turner and B. K. Mann, *J. Biomed. Mater. Res., Part A*, 2005, **72**, 91–97.

49 A. Banerjee, M. Arha, S. Choudhary, R. S. Ashton, S. R. Bhatia, D. V. Schaffer and R. S. Kane, *Biomaterials*, 2009, **30**, 4695–4699.

50 A. S. van Oosten, X. Chen, L. Chin, K. Cruz, A. E. Patteson, K. Pogoda, V. B. Shenoy and P. A. Janmey, *Nature*, 2019, **573**, 96–101.

51 S. Budday, G. Sommer, C. Birkl, C. Langkammer, J. Haybaeck, J. Kohnert, M. Bauer, F. Paulsen, P. Steinmann, E. Kuhl and G. A. Holzapfel, *Acta Biomater.*, 2017, **48**, 319–340.

52 J. Groll, T. Boland, T. Blunk, J. A. Burdick, D.-W. Cho, P. D. Dalton, B. Derby, G. Forgacs, Q. Li, V. A. Mironov, L. Moroni, M. Nakamura, W. Shu, S. Takeuchi, G. Vozzi, T. B. Woodfield, T. Xu, J. J. Yoo and J. Malda, *Biofabrication*, 2016, **8**, 013001.

53 L. Moroni, T. Boland, J. A. Burdick, C. De Maria, B. Derby, G. Forgacs, J. Groll, Q. Li, J. Malda, V. A. Mironov, C. Mota, M. Nakamura, W. Shu, S. Takeuchi, T. B. Woodfield, T. Xu, J. J. Yoo and G. Vozzi, *Trends Biotechnol.*, 2018, **36**, 384–402.

54 L. Ouyang, R. Yao, Y. Zhao and W. Sun, *Biofabrication*, 2016, **8**, 035020.

55 K. Hölzl, S. Lin, L. Tytgat, S. Van Vlierberghe, L. Gu and A. Ovsianikov, *Biofabrication*, 2016, **8**, 032002.

56 Y. Zhao, Y. Li, S. Mao, W. Sun and R. Yao, *Biofabrication*, 2015, **7**, 1–11.

57 N. Paxton, W. Smolan, T. Böck, F. Melchels, J. Groll and T. Jungst, *Biofabrication*, 2017, **9**, 044107.

58 V. Mironov, T. Boland, T. Trusk, G. Forgacs and R. R. Markwald, *Trends Biotechnol.*, 2003, **21**, 157–161.

59 D. B. Kolesky, R. L. Truby, A. S. Gladman, T. A. Busbee, K. A. Homan and J. A. Lewis, *Adv. Mater.*, 2014, **26**, 3124–3130.

60 T. Distler, F. Ruther, A. R. Boccaccini and R. Detsch, *Macromol. Biosci.*, 2019, **19**, 1–13.

61 Y. S. Zhang and A. Khademhosseini, *Science*, 2017, **356**, 1–10.

62 I. Apsite, J. M. Uribe, A. F. Posada, S. Rosenfeldt, S. Salehi and L. Ionov, *Biofabrication*, 2020, **12**, 015016.

63 T. R. Cox and C. Madsen, *Bio-Protoc.*, 2017, 7(1), e2101.

64 R. L. Mauck, S. L. Seyhan, G. A. Ateshian and C. T. Hung, *Ann. Biomed. Eng.*, 2002, **30**, 1046–1056.

65 Z. Tan, D. Dini, F. R. y. Baena and A. E. Forte, *Mater. Des.*, 2018, **160**, 886–894.

66 A. E. Forte, S. Galvan, F. Manieri, F. R. y. Baena and D. Dini, *Mater. Des.*, 2016, **112**, 227–238.

67 A. Leibinger, A. E. Forte, Z. Tan, M. J. Oldfield, F. Beyrau, D. Dini and F. R. y. Baena, *Ann. Biomed. Eng.*, 2015, **44**, 2442–2452.

68 R. Detsch, B. Sarker, T. Zehnder, G. Frank and A. R. Boccaccini, *Mater. Today*, 2015, **18**, 590–591.

69 S. N. Pawar and K. J. Edgar, *Biomaterials*, 2012, **33**, 3279–3305.

70 Ø. Arlov, E. Öztürk, M. Steinwachs, G. Skjåk-Bræk and M. Zenobi-Wong, *Eur. Cells Mater.*, 2017, **33**, 76–89.

71 M. Ø. Dalheim, J. Vanacker, M. A. Najmi, F. L. Aachmann, B. L. Strand and B. E. Christensen, *Biomaterials*, 2016, **80**, 146–156.

72 K. Hozumi and M. Nomizu, *Curr. Protoc. Cell Biol.*, 2018, **80**, 1–15.

73 Y. S. Hsueh, Y. S. Chen, H. C. Tai, O. Mestak, S. C. Chao, Y. Y. Chen, Y. Shih, J. F. Lin, M. J. Shieh and F. H. Lin, *Tissue Eng., Part A*, 2017, **23**, 185–194.

74 R. Silva, R. Singh, B. Sarker, D. G. Papageorgiou, J. A. Juhasz-Bortuzzo, J. A. Roether, I. Cicha, J. Kaschta, D. W. Schubert, K. Chrissafis, R. Detsch and A. R. Boccaccini, *Int. J. Biol. Macromol.*, 2018, **114**, 614–625.

75 S. Reakasame and A. R. Boccaccini, *Biomacromolecules*, 2018, **19**, 3–21.

76 K. H. Bouhadir, K. Y. Lee, E. Alsberg, K. L. Damm, K. W. Anderson and D. J. Mooney, *Biotechnol. Prog.*, 2001, **17**, 945–950.

77 C. G. Gomez, M. Rinaudo and M. A. Villar, *Carbohydr. Polym.*, 2007, **67**, 296–304.

78 B. Sarker, D. G. Papageorgiou, R. Silva, T. Zehnder, F. Gul-E-Noor, M. Bertmer, J. Kaschta, K. Chrissafis, R. Detsch and A. R. Boccaccini, *J. Mater. Chem. B*, 2014, **2**, 1470–1482.

79 B. Balakrishnan, M. Mohanty, A. C. Fernandez, P. V. Mohanan and A. Jayakrishnan, *Biomaterials*, 2006, **27**, 1355–1361.

80 B. Sarker, R. Singh, R. Silva, J. A. Roether, J. Kaschta, R. Detsch, D. W. Schubert, I. Cicha and A. R. Boccaccini, *PLoS One*, 2014, **9**, DOI: 10.1371/journal.pone.0107952.

81 B. Sarker, T. Zehnder, S. N. Rath, R. E. Horch, U. Kneser, R. Detsch and A. R. Boccaccini, *ACS Biomater. Sci. Eng.*, 2017, **3**, 1730–1737.

82 T. Zehnder, B. Sarker, A. R. Boccaccini and R. Detsch, *Biofabrication*, 2015, **7**, 025001.

83 T. Zehnder, A. Boccaccini and R. Detsch, *Biofabrication*, 2017, **9**, 25016.

84 T. Distler, A. A. Solistio, D. Schneidereit, O. Friedrich, R. Detsch and A. R. Boccaccini, *Biofabrication*, 2020, **12**, 045005.

85 N. Soltan, L. Ning, F. Mohabatpour, P. Papagerakis and X. Chen, *ACS Biomater. Sci. Eng.*, 2019, **5**, 2976–2987.

86 F. Ruther, T. Distler, A. R. Boccaccini and R. Detsch, *J. Mater. Sci.: Mater. Med.*, 2019, **30**, 1–14.

87 F. You, X. Wu, M. Kelly and X. Chen, *Bio-Des. Manuf.*, 2020, **3**, 48–59.

88 A. Weizel, T. Distler, D. Schneidereit, O. Friedrich, L. Bräuer, F. Paulsen, R. Detsch, A. R. Boccaccini, S. Budday and H. Seitz, *Acta Biomater.*, 2020, **118**, 113–128.

89 S. Hafeez, H. Ooi, F. Morgan, C. Mota, M. Dettin, C. van Blitterswijk, L. Moroni and M. Baker, *Gels*, 2018, **4**, 85.

90 S. Schwarz, S. Kuth, T. Distler, C. Gögele, K. Stölzel, R. Detsch, A. Bocaccini and G. Schulze-Tanzil, *Mater. Sci. Eng., C*, 2020, **116**, 111189.

91 S. Girardo, N. Traeber, K. Wagner, G. Cojoc, C. Herold, R. Goswami, R. Schluessler, S. Abuhattum, A. Taubenberger, F. Reichel, *et al.*, *J. Mater. Chem. B*, 2018, **6**, 6245–6261.

92 N. Traeber, K. Uhlmann, S. Girardo, G. Kesavan, K. Wagner, J. Friedrichs, R. Goswami, K. Bai, M. Brand, C. Werner, *et al.*, *Sci. Rep.*, 2019, **9**, 1–14.

93 A. V. Taubenberger, S. Girardo, N. Träber, E. Fischer-Friedrich, M. Kräter, K. Wagner, T. Kurth, I. Richter, B. Haller, M. Binner, D. Hahn, U. Freudenberg, C. Werner and J. Guck, *Adv. Biosyst.*, 2019, **3**, 1–16.

94 B. Fregin, F. Czerwinski, D. Biedenweg, S. Girardo, S. Gross, K. Aurich and O. Otto, *Nat. Commun.*, 2019, **10**, 1–11.

95 K. Wagner, S. Girardo, R. Goswami, G. Rosso, E. Ulbricht, P. Müller, D. Soteriou, N. Träber and J. Guck, *Soft Matter*, 2019, **15**, 9776–9787.

96 J. Schindelin, I. Arganda-Carreras, E. Frise, V. Kaynig, M. Longair, T. Pietzsch, S. Preibisch, C. Rueden, S. Saalfeld, B. Schmid, J. Y. Tinevez, D. J. White, V. Hartenstein, K. Eliceiri, P. Tomancak and A. Cardona, *Nat. Methods*, 2012, **9**, 676–682.

97 O. Otto, P. Rosendahl, A. Mietke, S. Golfier, C. Herold, D. Klaue, S. Girardo, S. Pagliara, A. Ekpenyong, A. Jacobi, M. Wobus, N. Töpfner, U. F. Keyser, J. Mansfeld, E. Fischer-friedrich and J. Guck, *Nat. Methods*, 2015, **12**, 199–202.

98 M. Mokbel, D. Mokbel, A. Mietke, N. Träber, S. Girardo, O. Otto, J. Guck and S. Aland, *ACS Biomater. Sci. Eng.*, 2017, **3**, 2962–2973.

99 G. A. Holzapfel, *Nonlinear Solid Mechanics: A Continuum Approach for Engineering Science*, John Wiley & Sons, Chichester, 2000, vol. 24.

100 R. W. Ogden, *Proc. R. Soc. London, Ser. A*, 1972, **326**, 565–584.

101 C. M. Madl, B. L. Lesavage, R. E. Dewi, C. B. Dinh, R. S. Stowers, M. Khariton, K. J. Lampe, D. Nguyen, O. Chaudhuri, A. Enejder and S. C. Heilshorn, *Nat. Mater.*, 2017, **16**, 1233–1242.

102 H. P. Lee, L. Gu, D. J. Mooney, M. E. Levenston and O. Chaudhuri, *Nat. Mater.*, 2017, **16**, 1243–1251.

103 O. Chaudhuri, L. Gu, M. Darnell, D. Klumpers, S. A. Bencherif, J. C. Weaver, N. Huebsch and D. J. Mooney, *Nat. Commun.*, 2015, **6**, 1–7.

104 H. Park and K. Y. Lee, *J. Biomed. Mater. Res., Part A*, 2014, **102**, 4519–4525.

105 P. S. Braccini I, *Biomacromolecules*, 2001, **2**, 1089–1096.

106 F. Di Lorenzo and S. Seiffert, *Polym. Chem.*, 2015, **6**, 5515–5528.

107 A. Mietke, O. Otto, S. Girardo, P. Rosendahl, A. Taubenberger, S. Golfier, E. Ulbricht, S. Aland, J. Guck and E. Fischer-Friedrich, *Biophys. J.*, 2015, **109**, 2023–2036.

108 P. H. Wu, D. R. B. Aroush, A. Asnacios, W. C. Chen, M. E. Dokukin, B. L. Doss, P. Durand-Smet, A. Ekpenyong, J. Guck, N. V. Guz, P. A. Janmey, J. S. Lee, N. M. Moore, A. Ott, Y. C. Poh, R. Ros, M. Sander, I. Sokolov, J. R. Staunton, N. Wang, G. Whyte and D. Wirtz, *Nat. Methods*, 2018, **15**, 491–498.

109 P. Kollmannsberger and B. Fabry, *Annu. Rev. Mater. Res.*, 2011, **41**, 75–97.

110 I. E. Collier, S. M. Wilhelm, A. Z. Eisen, B. L. Marmer, G. A. Grant, J. L. Seltzer, A. Kronberger, C. He, E. A. Bauer and G. I. Goldberg, *J. Biol. Chem.*, 1988, **263**, 6579–6587.

111 T. Xia, K. Akers, A. Z. Eisen and J. L. Seltzer, *Biochim. Biophys. Acta, Protein Struct. Mol. Enzymol.*, 1996, **1293**, 259–266.

112 B. Lelongt, G. Trugnan, G. Murphy and P. M. Ronco, *J. Cell Biol.*, 1997, **136**, 1363–1373.

113 O. Lieleg, K. M. Schmoller, M. M. A. E. Claessens and A. R. Bausch, *Biophys. J.*, 2009, **96**, 4725–4732.

114 A. Atala and J. Yoo, *Essentials of 3D Biofabrication and Translation*, Elsevier, 1st edn, 2015, pp. 440.

115 J. Malda, J. Visser, F. P. Melchels, T. Jüngst, W. E. Hennink, W. J. A. Dhert, J. Groll and D. W. Hutmacher, *Adv. Mater.*, 2013, **25**, 5011–5028.

116 S. J. Müller, E. Mirzahossein, E. N. Iftekhar, C. Bächer, S. Schrüfer, D. W. Schubert, B. Fabry and S. Gekle, *PLoS One*, 2020, **15**, 1–15.

117 B. Xue, V. Kozlovskaya, F. Liu, J. Chen, J. F. Williams, J. Campos-Gomez, M. Saeed and E. Kharlampieva, *ACS Appl. Mater. Interfaces*, 2015, **7**, 13633–13644.

118 S. Freiberg and X. X. Zhu, *Int. J. Pharm.*, 2004, **282**, 1–18.

119 N. K. Varde and D. W. Pack, *Expert Opin. Biol. Ther.*, 2004, **4**, 35–51.

120 K. K. Kim and D. W. Pack, Microspheres for Drug Delivery in *BioMEMS and Biomedical Nanotechnology*, ed. M. Ferrari, A. P. Lee and L. J. Lee, Springer, Boston, MA. DOI: 10.1007/978-0-387-25842-3_2.

121 R. Sharma, I. P. Smits, L. De La Vega, C. Lee and S. M. Willerth, *Front. Bioeng. Biotechnol.*, 2020, **8**, 1–12.

122 M. Bahadoran, A. Shamloo and Y. D. Nokoorani, *Sci. Rep.*, 2020, **10**, 7–9.

123 Y. Karamzadeh, A. Ansari Asl and S. Rahmani, *J. Appl. Polym. Sci.*, 2020, **137**, 1–11.

124 S. Kühn, J. Sievers, A. Stoppa, N. Träber, R. Zimmermann, P. B. Welzel and C. Werner, *Adv. Funct. Mater.*, 2020, **30**, DOI: 10.1002/adfm.201908857.

125 T. Lühmann and H. Hall, *Materials*, 2009, **2**, 1058–1083.

126 C.-C. Lin, P. D. Boyer, A. A. Aimetti and K. S. Anseth, *J. Controlled Release*, 2010, **142**, 384–391.

127 L. M. Weber, C. G. Lopez and K. S. Anseth, *J. Biomed. Mater. Res., Part A*, 2009, **90**, 720–729.

128 E. Axpe, D. Chan, G. S. Offeddu, Y. Chang, D. Merida, H. L. Hernandez and E. A. Appel, *Macromolecules*, 2019, **52**, 6889–6897.

129 V. Crosignani, A. Dvornikov, J. S. Aguilar, C. Stringari, R. Edwards, W. W. Mantulin and E. Gratton, *J. Biomed. Opt.*, 2012, **17**, 116023.